

Short-period pulsating hot-subdwarf stars observed by TESS

II. Northern ecliptic hemisphere

A.S. Baran^{1,2}, S. Charpinet³, R.H. Østensen^{2,4}, M.D. Reed², V. Van Grootel⁵, C. Lyu³, J.H. Telting^{6,7}, P. Németh^{8,9}

¹ Astronomical Observatory, University of Warsaw, Al. Ujazdowskie 4, 00-478 Warszawa, Poland

² ARDASTELLA Research Collaboration, Missouri State University, Springfield, MO 65897, USA

³ IRAP, CNRS, UPS, CNES, Université de Toulouse, 14 av. Edouard Belin, 31400 Toulouse, France

⁴ Recogito AS, Storgaten 72, N-8200 Fauske, Norway

⁵ Space sciences, Technologies and Astrophysics Research (STAR) Institute, Université de Liège, 19C Allée du 6 Août, B-4000 Liège, Belgium

⁶ Nordic Optical Telescope, Rambla José Ana Fernández Pérez 7, 38711 Breña Baja, Spain

⁷ Department of Physics and Astronomy, Aarhus University, NyMunkegade 120, DK-8000 Aarhus C, Denmark

⁸ Astronomical Institute of the Czech Academy of Sciences, Fričova 298, CZ-251 65 Ondřejov, Czech Republic

⁹ Astroserver.org, Fő tér 1, 8533 Malomsok, Hungary

ABSTRACT

We present results of a continuation of our Transiting Exoplanet Survey Satellite (TESS) search for short-period pulsations in compact stellar objects observed during Years 2 and 4 of the TESS mission that targeted the northern ecliptic hemisphere. For many of the targets, we exploit unpublished spectroscopic data to confirm or determine the object's spectral classification. From the TESS photometry, we identify 50 short-period hot-subdwarf pulsators, including 35 sdB and 15 sdOB stars. The sample contains 26 pulsators not known before the TESS mission. Nine stars show signals at both low and high frequencies, and are therefore “hybrid” pulsators. For each pulsator, we report the list of prewhitened frequencies and we show amplitude spectra calculated from the TESS data. We attempt to identify possible multiplets caused by stellar rotation, and we report five candidates with rotation periods between 11 and 46 d. Having the search for p-mode pulsating hot subdwarfs in TESS Sectors 1–60 done, we discuss the completeness of the study, as well as instability strip and the evolutionary status of the stars we found. We also compare the distribution of pulsation periods as a function of effective temperature and surface gravity with theoretical predictions. We find that the percentage of undetected pulsators in the TESS mission increases with decreasing brightnesses of stars, reaching 25% near the 15th magnitude. When comparing the distribution of hot subdwarfs in the $\log g$ - T_{eff} plane with stellar models, we underline the importance of a proper treatment of the hydrogen-rich envelope composition (strongly affected by microscopic diffusion processes). We also emphasize that the stellar mass is a significant factor in understanding the instability strip. The p-mode instability strip is confirmed to be narrower than predicted by non-adiabatic calculations based on models incorporating equilibrium between gravitational settling and radiative levitation for iron. This implies that competing mixing processes ignored in these models must play a role to reduce the amount of levitating iron in the stellar envelope. Interestingly, we find that the coolest p-mode pulsators with $T_{\text{eff}} \lesssim 30,000$ K (including the hybrid ones) tend to cluster around the Terminal Age of the Extreme Horizontal Branch of canonical mass ($\sim 0.47 M_{\odot}$), a trend expected from the non-adiabatic pulsation calculations. Otherwise, the overall pulsation period distributions tend to reproduce the predicted trends in T_{eff} and $\log g$.

Key words. Stars: oscillations - Asteroseismology - Stars: variable stars - stars: horizontal-branch - subdwarfs

1. Introduction

Baran et al. (2023, hereafter: Paper I) reported their detection of 43 hot-subdwarf pressure (p) mode pulsators in the southern ecliptic hemisphere observed with the Transiting Exoplanet Survey Satellite (TESS). The sample includes 32 subdwarf B (sdB) stars, eight subdwarf OB (sdOB) stars, two subdwarf O (sdO) stars, and, significantly, one He-sdOB star, which is the first of this kind to show short-period pulsations. An introduction to all types of hot subdwarfs are provided in Paper I.

We continued our effort to search for hot-subdwarf p-mode pulsators in the northern ecliptic hemisphere observed by TESS. Our ultimate goal is to report the census of the p-mode-dominated hot-subdwarf stars surveyed by the TESS satellite, along with an ensemble analysis on the presence of p-mode pulsators among hot subdwarfs.

2. Classification spectra

To verify or establish the spectral classification for some of the objects, new spectra were obtained using the ALFOSC spectrograph on the 2.56 m Nordic Optical Telescope (NOT). We mainly used grism #18 that samples the Balmer series from H_{β} to shorter wavelengths, spanning 345–535 nm, and we used a 1-arcsec slit resulting in $R = 1000$ spectral resolution. These spectra also serve to obtain estimates of the effective temperature, surface gravity and surface He/H, using the classical LTE model atmospheres of Heber et al. (2000). The obtained values are quoted in the context of the individual stars.

3. TESS photometry

We follow the same approach as explained in Paper I. Basically, we downloaded all available data of our targets from the Barbara

A. Mikulski Archive for Space Telescopes (MAST)¹. Our preference is to use the USC (ultra-short cadence of 20 s integration) data, if available, with which the entire p-mode frequency range is sampled. In the case of the SC (short cadence of 120 s) data, the Nyquist frequency (at 4167 μHz) is in the middle of the p-mode region and aliasing becomes a serious issue. We used PD-CSAP_FLUX, which is corrected for on-board systematics and neighbors' contributions to the overall flux. We clipped fluxes at 4.5σ to remove outliers, de-trended long-term variations (on the order of days) with spline fitting, and calculated the amplitude of the flux variations using the relation $A[\text{ppt}] = 1000 * (\text{flux} / \langle \text{flux} \rangle - 1)$, where ppt is parts-per-thousand.

4. Fourier analysis

We used the same prewhitening techniques with a detection threshold as described in Paper I. Based on results presented by Baran & Koen (2021), we adopted a detection threshold at signal-to-noise (S/N) of 4.5 times the median noise level to both the SC and USC data sets, regardless of the data coverage. Nevertheless, frequencies with $S/N \leq 5.5$ (corresponding to a FAP = 0.1%) should be considered tentative. To search for significant signal in the amplitude spectra, we used the FELIX package (Charpinet et al. 2010; Zong et al. 2016) and other dedicated scripts. We followed the same procedure as explained in Paper I. At first, an automatic search was performed, looking for significant variations beyond 1 500 μHz where p-modes are usually found. Then, an individual check was carried out to establish if detected variations are indeed consistent with p-mode pulsations. We detected signals in the p-mode region in 50 hot subdwarfs. Twelve targets were observed only in the SC mode, while 38 were observed in the USC mode. We found 11 new detections in SC data and 16 new detections in USC data, while the remaining one (SC) and 22 (USC) hot-subdwarf pulsators were already known prior to the TESS mission. We present the list of all p-mode hot subdwarf pulsators in Table 1. This table also provides the spectral type (SpT), either from the literature or from new spectroscopy that we acquired recently. The classification convention we applied is explained in Paper I, basically we marked those stars with detectable He I, or no He I lines at all, with a B class. Those stars with detectable He II at 4686 \AA with class OB, and those stars with strong He II and no He I with class O. Below we describe each target, including previously-published pulsation properties, followed by amplitude spectra and the list of frequencies detected from the TESS light curves.

4.1. Targets observed in the SC mode

For stars with SC mode data, the Nyquist frequency is at 4167 μHz . As in Paper I, we decided to prewhiten frequencies that are found in the super-Nyquist region. We tried to discern sub- from super-Nyquist, by first relying on previously-published results for known pulsators and then using a combination of amplitude, multi-sector observations (if available), and peak shape in the Fourier transform (FT). We show amplitude spectra of SC-observed pulsating subdwarf B stars (sdBV) in Figure 1 and A.1 and provide the seismic properties of the detected pulsation frequencies, f_1 to f_N in Table 2, as well as any detected binary orbital signal as Ω and its harmonic 2Ω .

TIC 968226 (PHL 211) is a new sdB pulsator. The spectral classification was revealed by Kilkeny (1984), who marked it as an sdB star based on Strömgren indices. Our fit to a spectrum taken with the NOT in 2022 gives $T_{\text{eff}} = 28\,982(198)\text{ K}$, $\log(g/\text{cm s}^{-2}) = 5.42(3)$ and $\log(n(\text{He})/n(\text{H})) = -3.15(9)$, and we classified the star as an sdB. TESS observed the star during Sector 42. We detected two frequencies in the p-mode region provided in Table 2 and shown in Fig. 1.

TIC 16993518 (FBS 1539+355) is a new sdOB pulsator. Pérez-Fernández et al. (2016) found the star as a hot subdwarf candidate with $T_{\text{eff}} = 32\,500\text{ K}$. Later, based on photometry, Geier et al. (2017) classified the star as an sdB. Our fit to a spectrum taken with the NOT in 2022 gives $T_{\text{eff}} = 32\,194(187)\text{ K}$, $\log(g/\text{cm s}^{-2}) = 5.37(4)$ and $\log(n(\text{He})/n(\text{H})) = -2.27(9)$, and we classified the star as an sdOB. TESS observed the star during Sector 51. We detected three frequencies in the p-mode region shown in Fig. 1, with frequencies in Table 2.

TIC 85145647 (FBS 0725+623) is a new sdB pulsator. Based on photometry, Geier et al. (2017) classified the star as an sdB. Our fit to a spectrum taken with the INT in 2014 gives $T_{\text{eff}} = 32\,287(656)\text{ K}$, $\log(g/\text{cm s}^{-2}) = 5.41(12)$ and $\log(n(\text{He})/n(\text{H})) = -3.03(39)$, indicating an sdB classification. TESS observed the star during Sectors 20 and 47. We detected seven frequencies in Sector 20 and two frequencies in Sector 47, which differed in amplitude. We show the amplitude spectrum calculated from Sector 20 data in Fig. 1, and we list the prewhitened frequencies in data from both Sectors in Table 2. Three frequencies f_2 , f_3 and f_4 , make a slightly asymmetric triplet. The signal-to-noise (S/N) ratio of f_4 is only 3.6, which may not be an intrinsic signal. The splittings on both sides are 1.11 and 0.99 μHz and assuming the splitting is caused by rotation, the average rotation period is 11.0(7) days.

TIC 97286494 (GALEX J081110.8+273420) is a new sdB pulsator. Based on photometry, Geier et al. (2017) classified the star as an sdB+F. TESS observed the star during Sectors 44–47 from which we detected only one frequency in the p-mode region. We show the amplitude spectrum in Fig. 1, and list the prewhitened frequency in Table 2.

TIC 154818961 (*Gaia* DR3 1935962732084366592) is a new sdB pulsator. Our fit to a spectrum taken with the NOT in 2023 gives $T_{\text{eff}} = 28\,330(281)\text{ K}$, $\log(g/\text{cm s}^{-2}) = 5.29(4)$ and $\log(n(\text{He})/n(\text{H})) = -1.71(5)$, and we classified the star as an sdB. TESS observed the star during Sector 57. We detected three frequencies and based on amplitudes and profiles we selected those in the sub-Nyquist region. We interpret the two low frequencies to be a binary frequency and its first harmonic. We show the amplitude spectrum in Fig. 1, and list the prewhitened frequencies in Table 2. The middle panel shows an additional comb of low amplitude frequencies; we found that TIC 2041859698 (*Gaia* DR3 1935962732084366464) is the source of those frequencies, which we interpret to be caused by eclipses. We estimate the orbital period of this eclipsing binary system to be near 1.5 d.

TIC 157141133 (*Gaia* DR3 6904512841490841472) is a new sdB pulsator. Our fit to a spectrum taken with the ING in 2014 gives $T_{\text{eff}} = 31\,076(207)\text{ K}$, $\log(g/\text{cm s}^{-2}) = 5.60(4)$ and

¹ archive.stsci.edu

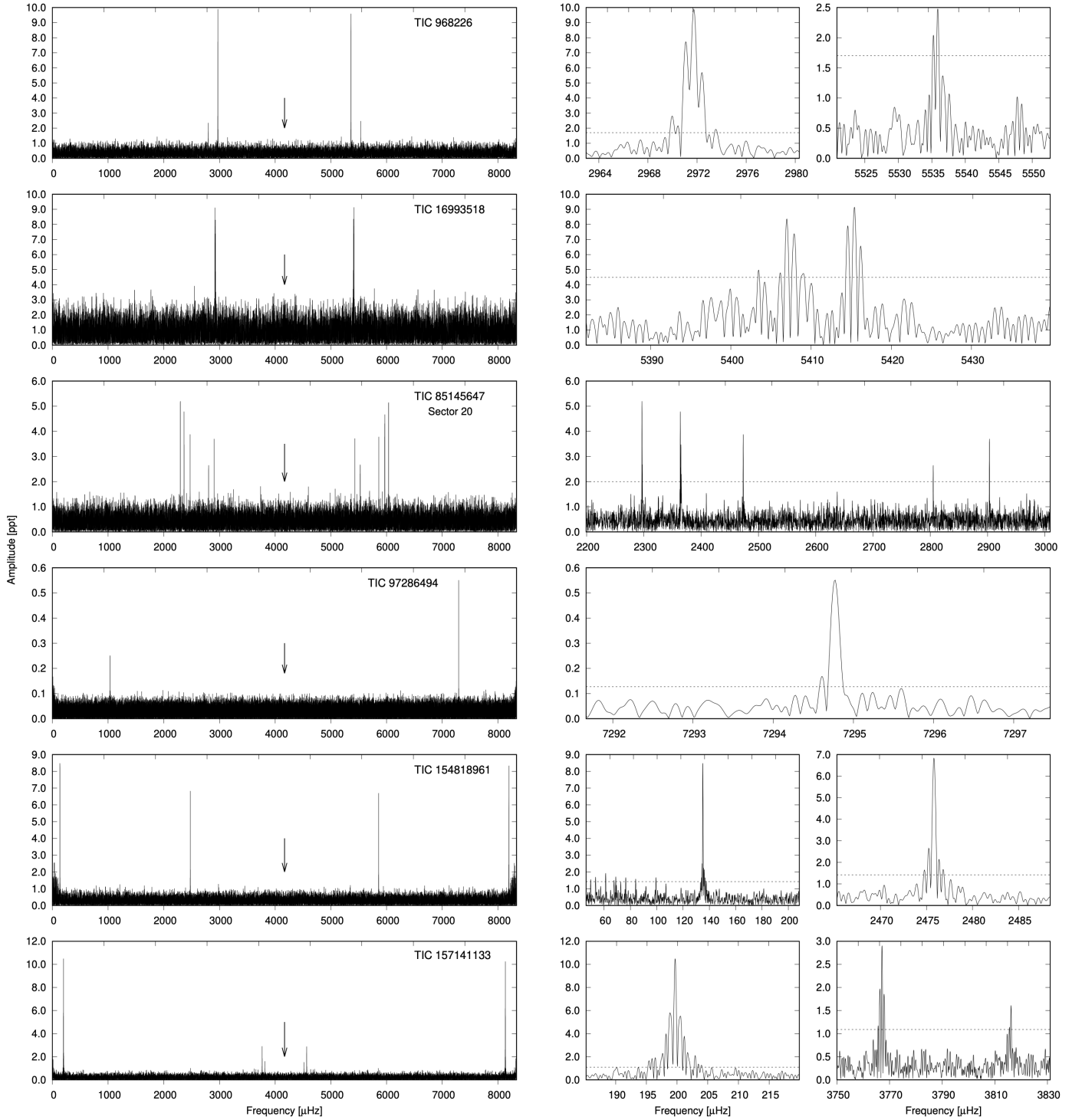


Fig. 1. Amplitude spectra of the targets observed in the SC mode. If sector is not specified, we included all data. *Left panels:* Frequency range, up to twice the Nyquist frequency. The arrows point at the Nyquist frequency of 4166.67 μHz . *Right panels:* Close-ups of the detected frequencies.

$\log(n(\text{He})/n(\text{H})) = -2.97(16)$, and we classified the star as an sdB. TESS observed the star during Sector 54. We detected three frequencies in the sub-Nyquist region. Frequency f_1 is likely a binary signature. We show the amplitude spectrum in Fig. 1, and the prewhitened frequencies in Table 2.

TIC 186484490 (FBS 0117+396) is a known sdB pulsator. It was originally identified as sdB-O in the First Byurakan Sky Survey (Abrahamian et al. 1990). Østensen et al. (2013) derived

atmospheric parameters and classified the star as an sdB. The same authors reported a discovery of the star to be an sdB+dM binary system with a pulsating primary. Two high and eight low frequency signals were reported and the orbital period was estimated to be 0.252013(13) days. The binarity was confirmed with radial velocity data. TESS observed the star during Sector 17. We detected a binary frequency and its first harmonic. The orbital period we measured is 0.251966(23) days and we detected only one high frequency signal, frequency f_1 reported by Østensen et al. (2013), and in the sub-Nyquist region. We show the ampli-

tude spectrum in Fig. A.1, and list the prewhitened frequencies in Table 2.

TIC 199715319 (PG 1656+553) is a new sdB pulsator. The star was classified as an sdB star in the Palomar-Green (PG) survey (Green et al. 1986) and later confirmed by Kilkenny et al. (1988). Our fit to a spectrum taken with the NOT in 2023 gives $T_{\text{eff}} = 28\,144(310)$ K, $\log(g/\text{cm s}^{-2}) = 5.32(4)$ and $\log(n(\text{He})/n(\text{H})) = -3.15(10)$, and we classified the star as an sdB. TESS observed the star during Sectors 40, 49–53, 56–57 and 59. We detect only one frequency, listed in Table 2 and show the amplitude spectrum calculated from all sectors except 40 in Fig. A.1.

TIC 222892604 (LS IV+06° 5) is a new sdB pulsator. Nassau & Stephenson (1963) classified it as a main-sequence B star. We obtained a NOT spectrum in 2022 and re-classify it as an sdB star. Our fit gives $T_{\text{eff}} = 30\,363(188)$ K, $\log(g/\text{cm s}^{-2}) = 5.47(3)$ and $\log(n(\text{He})/n(\text{H})) = -3.08(13)$. TESS observed the star during Sector 54. We detected five frequencies with two of them being close to each other, possibly part of a multiplet. The frequency splitting is 0.5039 μHz , giving a rotation period of either 23 or 46 days (for Δm of 1 or 2, respectively). We show the amplitude spectrum in Fig. A.1, and list the prewhitened frequencies in Table 2.

TIC 248776104 (PG 2052–003) is a new sdB pulsator. The star was classified as an sdB star in the Palomar-Green (PG) survey (Green et al. 1986). Our fit to a spectrum taken with the NOT in 2022 gives $T_{\text{eff}} = 32\,891(205)$ K, $\log(g/\text{cm s}^{-2}) = 5.52(4)$ and $\log(n(\text{He})/n(\text{H})) = -2.89(14)$, and we classified the star as an sdB. TESS observed the star during Sector 55. We detected two frequencies, which we list in Table 2 and show the amplitude spectrum in Fig. A.1.

TIC 331656308 (FBS 0433+759) is a new sdB pulsator. Our fit to a spectrum taken with the NOT in 2022 gives $T_{\text{eff}} = 28\,411(230)$ K, $\log(g/\text{cm s}^{-2}) = 5.36(3)$ and $\log(n(\text{He})/n(\text{H})) = -2.95(11)$, and we classified the star as an sdB. TESS observed the star during Sectors 52, 53 and 59. The frequency content significantly varies over time and we decided to analyze each contiguous set separately. Therefore, Sectors 52 and 53 were merged but Sector 59 data were treated separately. We detected four and five frequencies in the former and latter data sets, respectively. One/three frequencies were detected in the g-mode region, which makes the star a hybrid pulsator. The total power of p-mode signals during Sector 59 is smaller than during Sectors 52–53, while the power of g-mode signals are quite opposite. Energy transferred between modes through nonlinear coupling is a possible explanation for such a variable pulsation spectrum (Zong et al. 2016). We show the amplitude spectrum for Sector 59 data in Fig. A.1, and we separately list the prewhitened frequencies from both data sets in Table 2.

TIC 392092589 (Ton 4) is a new sdB pulsator. It was classified as a hot subdwarf by Pérez-Fernández et al. (2016). Our fit to a spectrum taken with the NOT in 2015 gives $T_{\text{eff}} = 27\,654(280)$ K, $\log(g/\text{cm s}^{-2}) = 5.40(4)$ and $\log(n(\text{He})/n(\text{H})) = -2.97(10)$, and we confirm the sdB classification. TESS observed the star during Sectors 44–46. We detected

four frequencies, three g-modes and one p-mode. Two additional g-mode frequencies may be seen in the middle panel, however their amplitudes do not meet our detection limit. We show the amplitude spectrum in Fig. A.1, and list the prewhitened frequencies in Table 2.

4.2. Targets observed in the USC mode

For all targets observed in the USC mode, there is also corresponding SC data available. In addition, some targets listed below were observed during specific sectors (1–13) in SC mode as USC was not available. The Nyquist frequency of USC data, $25,000$ μHz , is well beyond expected pulsation frequencies and so USC provides us with a unique frequency identification. As such we decided not to include any SC data in this paper, even those taken in sectors without available USC data. Table 1 provides detailed sector information, including sectors with SC data that were not used in our analyses. We show the amplitude spectra of SC-observed sdBV stars in Figures 2 through A.6 and provide the seismic properties in Table 3.

Table 1. The list of pulsating hot subdwarfs found in the TESS data. No USC data were available prior to Sector 27, hence data in sectors marked in parentheses were not used in our analysis. New pulsators are marked with **bold** font.

	TIC	Sector	SpT	
SC targets	968226	42	sdB	
	16993518	51	sdOB	
	85145647	20,47	sdB	
	97286494	44–47	sdB	
	154818961	57	sdB	
	157141133	54	sdB	
	186484490	17	sdB	
	199715319	40,49–53,56,57,59	sdB	
	222892604	54	sdB	
	248776104	55	sdB	
	331656308	52,53,59	sdB	
	392092589	44–46	sdB	
	USC targets	4632676	49	sdOB
		26291471	51	sdOB
55753808		(21),(22),41,48	sdOB	
56863037		(21),47	sdB	
60985176		(17),42,43	sdOB	
63168679		44,46	sdOB	
68495594		(20),44,45,60	sdOB	
82359147		(24)–(26),51,52	sdB	
88484868		(20),47,60	sdB	
88565376		(20),47,60	sdB	
90960668		56	sdB	
114196505		54	sdB	
136975077		(15),(16),55,56	sdB	
137502282		(20),40,47,53,60	sdOB	
138618727		(14),(15),(21),41,48	sdB	
142398823		41,48,49	sdB	
159644241		(14),(15),40,41,54,55	sdB	
165312944		(15),(22),48,49	sdB	
166054500		(22),(23),48,49	sdB	
175402069		(23),46,50	sdB	
178081355		58	sdOB	
191442416		(17),57	sdB	
202354658		(15),(16),(18),(22)–(24), 48–51,58	sdB	
207440586		(16),(22)–(25),49–52,56	sdOB	
219492314		(24),(25),51,52	sdOB	
240868270		(17),(18),58	sdOB	
266013993		42,43	sdB	
273255412		54	sdB	
284692897		40,41,54	sdB	
309807601		49,50	sdB	
310937915		42	sdOB	
355754830		60	sdB	
357232133		47,60	sdOB	
364966239		41,47,54–57,60	sdOB	
397595169		56	sdB	
424720852		(14)–(16),(20),(23), 40,41,50,54–57,60	sdB	
441725813		(14)–(25), 40,41,47–52,55–60	sdB	
471015194		(14),(16),(17),(20),(23), 40,41,47,50,54–57,60	sdB	

Table 2. List of frequencies detected in the targets observed only with the SC. If sector is not specified, we included all data.

ID	Frequency [μ Hz]	Period [sec]	Amp. [ppt]	S/N
TIC 968226				
f_1	2971.735(8)	336.5038(9)	9.89(32)	26.4
f_2	5535.884(30)	180.6396(10)	2.51(32)	6.7
TIC 16993518				
f_1	5406.991(25)	184.9458(9)	8.8(9)	8.8
f_2	5409.845(48)	184.8482(16)	4.6(9)	4.6
f_3	5415.405(24)	184.6584(8)	9.1(9)	9.1
TIC 85145647 – Sector 20				
f_1	2296.635(17)	435.4197(33)	5.19(38)	11.7
f_2	2363.520(20)	423.0977(36)	4.61(38)	10.4
f_3	2364.626(30)	422.900(5)	3.26(38)	7.3
f_4	2365.62(6)	422.723(10)	1.61(38)	3.6
f_5	2473.358(23)	404.3086(38)	3.87(38)	8.7
f_6	2805.127(34)	356.4900(43)	2.64(38)	6.0
f_7	2903.264(24)	344.4399(29)	3.69(38)	8.3
TIC 85145647 – Sector 47				
f_1	2296.617(20)	435.4231(39)	6.0(5)	9.7
f_2	2363.493(14)	423.1026(25)	8.6(5)	14.0
TIC 97286494				
f_1	7294.7690(26)	137.084532(48)	0.552(24)	19.7
TIC 154818961				
Ω	67.5236(34)	14809.6(7)	1.51(27)	4.8
2Ω	135.0472	7404.8	8.51(27)	26.9
f_1	2475.812(8)	403.9079(14)	6.84(27)	21.6
TIC 157141133				
f_1	199.6893(44)	5007.78(11)	10.49(21)	43.4
f_2	3767.119(16)	265.4549(11)	2.90(21)	12.0
f_3	3816.152(28)	262.0441(19)	1.63(21)	6.7
TIC 186484490				
Ω	45.9351(43)	21769.9(2.0)	56.3(1)	47.1
2Ω	91.8702	10884.95	8.6(1)	7.2
f_1	2965.506(26)	337.2105(29)	9.7(1)	8.1
TIC 199715319 – Sector 49 – 53,56,57,59				
f_1	2809.4228(16)	355.94500(21)	3.76(30)	10.8
TIC 222892604				
f_1	4968.6121(35)	201.26345(14)	10.03(11)	104.5
f_2	4969.116(6)	201.24306(23)	6.36(11)	66.2
f_3	4979.745(30)	200.8135(12)	0.62(8)	6.4
f_4	5038.476(13)	198.4727(5)	1.47(8)	15.3
f_5	5223.378(40)	191.4470(15)	0.47(8)	4.9
TIC 248776104				
f_1	3735.552(26)	267.6980(19)	5.4(6)	7.3
f_2	3838.819(42)	260.4968(29)	3.3(6)	4.5
TIC 331656308 – Sector 52 – 53				
f_1	109.235(12)	9154.5(1.0)	2.52(25)	8.4
f_2	2672.733(16)	374.1489(23)	1.91(25)	6.4
f_3	2810.7229(41)	355.7804(5)	7.44(25)	24.9
f_4	2874.6505(20)	347.86838(24)	15.43(25)	51.7
TIC 331656308 – Sector 59				
f_1	147.351(40)	6786.5(1.8)	1.69(27)	5.3
f_2	278.870(32)	3585.91(41)	2.09(27)	6.5
f_3	325.350(35)	3073.61(33)	1.94(27)	6.1
f_4	2810.714(8)	355.7815(10)	8.33(27)	26.1
f_5	2874.478(10)	347.8893(12)	6.62(27)	20.8
TIC 392092589				
f_1	214.340(13)	4665.49(27)	1.42(22)	5.4
f_2	284.692(9)	3512.57(11)	2.00(22)	7.6
f_3	308.856(11)	3237.75(11)	1.65(22)	6.3
f_4	2669.558(7)	374.5938(10)	2.42(22)	9.2

Table 3. List of frequencies we detected in the targets observed in the USC. If sector is not specified, we included all USC data.

ID	Frequency [μ Hz]	Period [sec]	Amplitude [ppt]	S/N
TIC 4632676				
Ω	4.420(25)	226244(1283)	4.26(44)	8.1
f_1	7279.068(34)	137.3802(6)	3.08(44)	5.9
TIC 26291471				
f_1	7186.374(38)	139.1522(7)	7.4(1)	5.6
TIC 55753808 – Sector 41				
f_1	7569.914(5)	132.10189(9)	23.3(5)	40.8
TIC 56863037				
f_1	5924.675(41)	168.7856(12)	1.81(33)	4.6
f_2	6035.540(31)	165.6853(8)	2.42(33)	6.2
f_3	6175.911(42)	161.9194(11)	1.79(33)	4.6
f_4	6189.800(43)	161.5561(11)	1.74(33)	4.5
f_5	6419.795(17)	155.76822(40)	4.52(33)	11.6
TIC 60985176				
f_1	6089.529(9)	164.21631(25)	5.89(45)	11.2
f_2	8353.720(22)	119.70715(31)	2.46(45)	4.7
f_3	15350.164(22)	65.14588(9)	2.42(45)	4.6
TIC 63168679				
f_1	6657.017(10)	150.21743(23)	0.59(9)	5.8
f_2	6657.4928(44)	150.20670(10)	1.44(9)	14.0
f_3	6657.976(5)	150.19579(12)	1.30(10)	12.7
f_4	6658.2676(44)	150.18922(10)	1.93(10)	18.8
f_5	6658.629(9)	150.18106(20)	0.79(10)	7.8
f_6	6856.7648(41)	145.84137(9)	1.41(9)	13.8
f_7	7129.6351(19)	140.259632(38)	3.16(9)	30.8
f_8	7130.2417(20)	140.247700(39)	3.06(9)	29.8
f_9	7337.6183(27)	136.284003(50)	2.15(9)	21.0
f_{10}	7339.831(10)	136.24292(18)	0.61(9)	5.9
TIC 82359147				
f_1	6891.368(21)	145.10908(45)	4.7(7)	5.4
f_2	7567.595(21)	132.14237(37)	4.8(7)	5.5
TIC 88484868 – Sector 47				
f_1	173.607(19)	5760.2(6)	1.43(12)	10.1
f_2	180.171(42)	5550.3(1.3)	0.67(12)	4.7
f_3	186.959(30)	5348.8(9)	0.91(12)	6.4
f_4	216.256(15)	4624.15(31)	1.90(12)	13.4
f_5	222.732(18)	4489.70(37)	1.53(12)	10.7
f_6	273.006(23)	3662.93(30)	1.23(12)	8.7
f_7	291.265(13)	3433.30(16)	2.09(12)	14.7
f_8	298.380(11)	3351.43(12)	2.54(12)	17.9
f_9	2721.901(5)	367.3903(7)	5.23(12)	36.9
f_{10}	2744.9768(31)	364.30180(42)	9.66(14)	68.1
f_{11}	2745.647(8)	364.2129(11)	3.81(15)	26.8
f_{12}	2746.415(11)	364.1111(14)	2.87(14)	20.2
TIC 88484868 – Sector 60				
f_1	123.997(35)	8064.7(2.3)	0.77(11)	5.9
f_2	173.569(21)	5761.4(7)	1.31(11)	10.1
f_3	180.323(25)	5545.6(8)	1.08(11)	8.3
f_4	186.933(34)	5349.5(10)	0.80(11)	6.2
f_5	216.309(18)	4623.01(39)	1.49(11)	11.4
f_6	222.719(22)	4489.96(44)	1.24(11)	9.6
f_7	273.024(32)	3662.68(42)	0.86(11)	6.6
f_8	291.230(12)	3433.71(14)	2.32(11)	17.9
f_9	298.360(6)	3351.66(7)	4.48(11)	34.5
f_{10}	317.579(22)	3148.82(22)	1.20(11)	9.3
f_{11}	343.986(45)	2907.10(38)	0.61(11)	4.7
f_{12}	2721.913(9)	367.3887(12)	3.34(12)	25.7

Table 3. continued.

ID	Frequency [μ Hz]	Period [sec]	Amplitude [ppt]	S/N
f ₁₃	2722.467(25)	367.3139(34)	1.22(12)	9.4
f ₁₄	2745.054(7)	364.2916(9)	13.27(37)	102.0
f ₁₅	2745.364(22)	364.2504(29)	4.23(36)	32.5
f ₁₆	2746.307(7)	364.1253(9)	4.53(15)	34.9
f ₁₇	3043.387(37)	328.5813(40)	0.73(11)	5.6
TIC 88565376 – Sector 47				
f ₁	2605.994(20)	383.7307(29)	6.7(6)	9.8
f ₂	2753.9552(43)	363.1141(6)	30.9(6)	45.1
TIC 88565376 – Sector 60				
f ₁	2605.988(21)	383.7317(31)	5.55(49)	9.7
f ₂	2753.939(6)	363.1163(8)	19.65(49)	34.5
TIC 114196505				
f ₁	106.727(40)	9369.7(3.5)	7.3(1)	4.6
f ₂	2649.222(9)	377.4693(13)	31.9(1)	20.3
TIC 136975077				
f ₁	5045.308(29)	198.2040(11)	0.88(17)	5.7
f ₂	5045.508(13)	198.1961(5)	1.94(17)	12.5
f ₃	5084.231(21)	196.6866(8)	0.71(13)	4.6
f ₄	5093.9751(34)	196.31034(13)	4.30(13)	27.8
f ₅	5212.068(12)	191.86243(45)	1.21(13)	7.8
f ₆	5413.021(7)	184.73971(23)	2.23(13)	14.4
f ₇	5481.8018(38)	182.42177(13)	3.89(13)	25.2
TIC 137502282 – Sector 60				
f ₁	6162.566(17)	162.27008(45)	3.59(25)	12.2
f ₂	7074.937(16)	141.34401(32)	3.91(25)	13.3
TIC 138618727 – Sector 41				
Ω	33.6846(13)	29687.1(1.1)	23.68(13)	155.6
2 Ω	67.3692	14843.55	1.90(13)	12.5
f ₁	2641.979(23)	378.5041(34)	1.30(13)	8.6
f ₂	2837.514(25)	352.4212(31)	1.21(13)	7.9
f ₃	2850.814(10)	350.7770(12)	3.16(13)	20.8
f ₄	2874.318(36)	347.9087(43)	0.89(13)	5.8
f ₅	2877.1565(29)	347.56538(35)	10.88(13)	71.5
f ₆	2878.653(30)	347.3847(36)	1.04(13)	6.8
f ₇	2906.269(22)	344.0838(26)	1.41(13)	9.3
TIC 138618727 – Sector 48				
Ω	33.6826(14)	29688.9(1.2)	23.40(15)	135.3
2 Ω	67.3652	14844.45	2.02(15)	11.7
f ₁	2641.965(36)	378.506(5)	0.92(15)	5.3
f ₂	2837.508(24)	352.4220(30)	1.38(15)	8.0
f ₃	2874.372(30)	347.9021(36)	1.14(15)	6.6
f ₄	2877.1608(28)	347.56486(34)	12.47(15)	72.1
f ₅	2878.659(23)	347.3839(28)	1.53(15)	8.8
f ₆	2906.243(22)	344.0868(27)	1.49(15)	8.6
TIC 142398823 – Sector 48 – 49				
f ₁	6934.738(17)	144.20156(36)	1.32(21)	5.3
f ₂	7771.846(11)	128.66956(18)	2.07(21)	8.4
TIC 159644241				
f ₁	5472.8591(15)	182.71985(5)	3.4(5)	5.4
f ₂	5760.1970(5)	173.605172(15)	10.2(5)	16.4
f ₃	5760.97251(48)	173.581804(14)	10.9(5)	17.4
TIC 165312944				
f ₁	5806.563(18)	172.2189(5)	0.48(8)	5.3
f ₂	6721.456(14)	148.77729(31)	1.12(10)	12.5
f ₃	6721.592(22)	148.77428(50)	0.70(10)	7.8
f ₄	6961.3781(16)	143.649717(32)	5.54(8)	61.5
f ₅	7488.717(16)	133.53423(28)	0.67(9)	7.4
f ₆	7489.4568(14)	133.521032(25)	7.97(10)	88.6
f ₇	7490.125(8)	133.50912(14)	1.30(9)	14.4

Table 3. continued.

ID	Frequency [μ Hz]	Period [sec]	Amplitude [ppt]	S/N
f ₈	7807.7404(34)	128.07803(6)	2.53(8)	28.2
f ₉	8169.0575(27)	122.413142(40)	3.25(8)	36.2
TIC 166054500				
1	6680.396(14)	149.69173(31)	1.00(12)	6.9
TIC 175402069 – Sector 46				
f ₁	5298.045(34)	188.7489(12)	1.16(17)	6.0
f ₂	5392.023(48)	185.4592(17)	1.43(21)	7.3
f ₃	5392.454(46)	185.4443(16)	1.50(21)	7.7
f ₄	5417.004(46)	184.6039(16)	0.87(17)	4.5
f ₅	5435.4698(46)	183.97674(15)	8.77(17)	45.0
f ₆	5444.324(21)	183.6775(7)	1.87(17)	9.6
f ₇	5470.650(37)	182.7936(12)	1.09(17)	5.6
f ₈	5562.301(27)	179.7817(9)	1.49(17)	7.7
f ₉	5585.651(25)	179.0302(8)	1.57(17)	8.1
f ₁₀	5760.736(16)	173.58894(50)	2.43(17)	12.4
f ₁₁	7071.184(31)	141.4190(6)	1.29(17)	6.6
TIC 175402069 – Sector 50				
f ₁	5219.087(47)	191.6044(17)	0.82(16)	4.5
f ₂	5298.072(24)	188.7479(9)	1.57(16)	8.6
f ₃	5369.360(40)	186.2420(14)	0.95(16)	5.2
f ₄	5435.4582(28)	183.97713(9)	13.76(16)	75.2
f ₅	5444.320(19)	183.6777(6)	2.06(16)	11.2
f ₆	5470.662(41)	182.7932(14)	0.93(16)	5.1
f ₇	5552.316(44)	180.1050(14)	0.88(16)	4.8
f ₈	5562.355(45)	179.7800(15)	0.85(16)	4.7
f ₉	5585.631(26)	179.0308(8)	1.50(16)	8.2
f ₁₀	5757.213(39)	173.6952(12)	0.99(16)	5.4
f ₁₁	5760.722(15)	173.58935(47)	2.48(16)	13.6
f ₁₂	7071.229(35)	141.4181(7)	1.10(16)	6.0
TIC 178081355				
f ₁	6022.331(35)	166.0487(10)	1.93(30)	5.5
f ₂	6668.937(39)	149.9489(9)	1.73(30)	5.0
f ₃	6902.357(11)	144.87806(24)	5.88(30)	16.8
TIC 191442416				
f ₁	4271.481(28)	234.1108(16)	4.8(7)	6.3
f ₂	5482.207(20)	182.4083(7)	6.7(7)	8.8
TIC 202354658 – Sector 48 – 51				
f ₁	3074.957(6)	325.2078(6)	1.45(16)	7.9
f ₂	3077.0481(10)	324.98680(10)	8.96(16)	48.8
f ₃	3079.130(7)	324.7670(7)	1.31(16)	7.1
f ₄	3088.414(7)	323.7908(7)	1.26(16)	6.9
f ₅	3090.5031(10)	323.57191(11)	9.36(16)	51.0
f ₆	3091.167(7)	323.5024(7)	1.43(16)	7.8
f ₇	3091.848(5)	323.4312(5)	1.81(17)	9.9
f ₈	3092.595(7)	323.3530(7)	1.30(17)	7.1
TIC 207440586 – Sector 56				
f ₁	6945.996(21)	143.96784(43)	2.20(20)	9.3
f ₂	6948.178(29)	143.9226(6)	1.59(20)	6.7
f ₃	7191.515(31)	139.0528(6)	1.49(20)	6.3
TIC 219492314				
f ₁	6936.109(5)	144.17305(11)	5.56(24)	20.1
TIC 240868270				
f _A	1.7226(34)	580530(1155)	2.212(35)	59.9
f _B	3.4117(15)	293105(125)	5.316(33)	144.1
f _C	6.4641(29)	154701(69)	2.685(32)	72.8
f ₁	6219.191(7)	160.79262(18)	1.096(32)	29.7
f ₂	6220.319(7)	160.76347(19)	1.048(32)	28.4
f ₃	6886.900(21)	145.20322(45)	0.367(33)	9.9
f ₄	6888.509(11)	145.16930(24)	0.692(33)	18.7

Table 3. continued.

ID	Frequency [μ Hz]	Period [sec]	Amplitude [ppt]	S/N
f ₅	7128.9861(26)	140.27240(5)	2.911(32)	78.9
TIC 266013993				
f ₁	5240.491(7)	190.82182(27)	2.08(13)	14.0
f ₂	5284.909(9)	189.21803(31)	1.75(13)	11.8
f ₃	5611.984(14)	178.19011(44)	1.08(13)	7.3
f ₄	7233.366(17)	138.24822(32)	0.90(13)	6.0
TIC 273255412				
f ₁	200.757(37)	4981.1(9)	0.59(10)	5.1
f ₂	1767.072(35)	565.908(11)	0.61(10)	5.3
f ₃	1822.727(7)	548.6286(21)	4.34(12)	37.7
f ₄	1823.391(8)	548.4287(24)	3.81(12)	33.2
f ₅	1883.332(7)	530.9737(19)	3.65(10)	31.8
f ₆	1884.891(37)	530.535(10)	0.67(10)	5.8
f ₇	1905.196(28)	524.880(8)	0.78(10)	6.8
f ₈	1934.090(7)	517.0389(17)	3.60(12)	31.3
f ₉	1934.7020(35)	516.8755(9)	6.71(12)	58.4
f ₁₀	1972.958(24)	506.853(6)	0.90(10)	7.8
f ₁₁	2059.224(7)	485.6199(16)	3.33(12)	29.0
f ₁₂	2060.167(21)	485.3975(50)	1.08(12)	9.4
f ₁₃	2141.805(8)	466.8960(17)	2.73(10)	23.8
f ₁₄	2214.0914(32)	451.6525(7)	7.73(11)	67.2
f ₁₅	2215.170(18)	451.4326(36)	1.40(11)	12.1
f ₁₆	2329.046(13)	429.3604(24)	1.65(10)	14.4
f ₁₇	2392.977(19)	417.8896(33)	1.14(10)	9.9
f ₁₈	2473.978(30)	404.2073(49)	0.72(10)	6.3
f ₁₉	2498.3133(39)	400.2700(6)	5.57(10)	48.5
f ₂₀	2520.811(31)	396.6978(48)	0.92(12)	8.0
f ₂₁	2521.894(37)	396.527(6)	0.82(12)	7.1
f ₂₂	2523.414(41)	396.289(6)	0.66(12)	5.7
f ₂₃	2524.833(43)	396.066(7)	0.54(11)	4.7
f ₂₄	2593.443(36)	385.588(5)	0.60(10)	5.2
f ₂₅	2658.533(39)	376.147(5)	1.01(12)	8.7
f ₂₆	2659.046(25)	376.0747(35)	1.56(12)	13.5
TIC 284692897 – Sector 40 – 41				
Ω	121.7120(7)	8216.115(48)	1.06(19)	4.7
2 Ω	243.4240	4108.0575	15.27(19)	67.5
f ₁	3665.134(15)	272.8413(11)	1.40(19)	6.2
f ₂	3733.129(10)	267.8718(7)	2.14(19)	9.5
f ₃	3792.730(14)	263.6623(10)	1.52(19)	6.7
f ₄	3823.710(15)	261.5261(10)	1.48(19)	6.6
f ₅	3885.889(18)	257.3414(12)	1.21(19)	5.3
f ₆	3908.570(5)	255.84805(34)	4.21(19)	18.6
f ₇	3924.770(18)	254.7920(12)	1.17(19)	5.2
f ₈	3933.711(18)	254.2129(11)	1.22(19)	5.4
f ₉	3992.693(21)	250.4575(13)	1.01(19)	4.5
f ₁₀	4053.126(21)	246.7231(13)	1.01(19)	4.5
f ₁₁	4129.329(13)	242.1701(8)	1.63(19)	7.2
f ₁₂	4168.217(17)	239.9108(10)	1.24(19)	5.5
f ₁₃	4177.108(15)	239.4001(8)	1.48(19)	6.6
f ₁₄	4179.068(21)	239.2878(12)	1.05(19)	4.7
TIC 309807601				
f ₁	6896.776(17)	144.99528(36)	1.87(28)	5.8
f ₂	7344.805(11)	136.15066(21)	2.87(28)	8.8
TIC 310937915				
f ₁	6963.373(33)	143.6086(7)	11.0(2)	6.2
TIC 355754830				
f ₁	275.756(20)	3626.39(26)	0.80(7)	10.3
f ₂	403.764(25)	2476.69(15)	0.64(7)	8.3
f ₃	453.478(37)	2205.18(18)	0.43(7)	5.5
f ₄	565.832(10)	1767.310(32)	1.53(7)	19.8

Table 3. continued.

ID	Frequency [μ Hz]	Period [sec]	Amplitude [ppt]	S/N
f ₅	3832.835(20)	260.9035(13)	0.81(7)	10.5
f ₆	3841.620(9)	260.3069(6)	2.24(8)	28.8
f ₇	3842.4635(27)	260.24971(18)	7.24(9)	93.4
f ₈	3843.2473(26)	260.19663(17)	6.72(9)	86.7
f ₉	3845.345(19)	260.0547(13)	0.91(7)	11.7
f ₁₀	3846.846(8)	259.9533(5)	2.59(9)	33.4
f ₁₁	3847.491(9)	259.9096(6)	2.50(9)	32.3
f ₁₂	3848.369(20)	259.8503(13)	0.94(8)	12.1
f ₁₃	3874.494(37)	258.0982(25)	0.42(7)	5.5
f ₁₄	4028.902(19)	248.2066(12)	0.84(7)	10.8
TIC 357232133 – Sector 47				
f ₁	6744.690(31)	148.2648(7)	1.98(27)	6.3
f ₂	7167.391(8)	139.52078(16)	7.21(27)	22.9
f ₃	8065.521(16)	123.98455(24)	4.00(27)	12.7
f ₄	8066.831(30)	123.96441(45)	2.10(27)	6.7
TIC 364966239 – Sectors 54 – 57,60				
f ₁	6568.4587(38)	152.24272(9)	0.91(10)	7.8
f ₂	6569.0255(17)	152.229581(40)	2.08(10)	17.7
f ₃	6569.608(6)	152.21609(15)	0.54(10)	4.6
f ₄	6787.6974(24)	147.32537(5)	1.40(10)	11.9
TIC 397595169				
f ₁	2824.115(33)	354.0932(41)	2.08(30)	5.8
f ₂	2860.889(33)	349.5417(40)	2.09(30)	5.9
TIC 424720852 – Sectors 40 – 41				
f ₁	105.593(13)	9470.3(1.2)	0.62(7)	7.4
f ₂	2469.440(17)	404.9501(28)	0.51(7)	6.1
f ₃	2469.752(15)	404.8990(25)	0.58(7)	6.9
f ₄	2470.079(8)	404.8453(13)	1.06(7)	12.8
f ₅	2662.554(18)	375.5792(25)	0.45(7)	5.4
f ₆	2680.773(5)	373.0268(7)	2.87(10)	34.4
f ₇	2681.0261(41)	372.9915(6)	5.78(8)	69.3
f ₈	2681.289(15)	372.9550(20)	1.11(9)	13.3
f ₉	2708.836(18)	369.1622(25)	0.44(7)	5.3
TIC 424720852 – Sectors 50,54 – 57,60				
f ₁	105.6188(34)	9468.01(30)	0.328(46)	6.1
f ₂	175.7895(27)	5688.62(9)	0.408(46)	7.6
f ₃	271.0415(46)	3689.47(6)	0.239(46)	4.5
f ₄	289.9835(36)	3448.472(43)	0.482(50)	9.0
f ₅	290.066(6)	3447.49(7)	0.308(50)	5.8
f ₆	309.8852(31)	3227.001(33)	0.353(46)	6.6
f ₇	2469.5573(31)	404.9309(5)	0.398(50)	7.4
f ₈	2469.6820(17)	404.91043(28)	0.727(50)	13.6
f ₉	2470.0434(11)	404.85119(18)	0.997(46)	18.6
f ₁₀	2662.5412(18)	375.58104(25)	0.620(46)	11.6
f ₁₁	2680.76199(49)	373.02827(7)	2.531(48)	47.3
f ₁₂	2681.02654(22)	372.991458(30)	5.852(47)	109.4
f ₁₃	2681.2944(10)	372.95420(14)	1.209(48)	22.6
f ₁₄	2708.8358(30)	369.16228(41)	0.367(46)	6.9
TIC 441725813 – Sectors 55 – 60				
f ₁	2755.5369(38)	362.9057(5)	0.098(9)	11.1
f ₂	2768.4702(24)	361.21032(31)	0.162(9)	18.2
f ₃	2769.1459(32)	361.12218(41)	0.122(9)	13.7
f ₄	2769.817(6)	361.0346(8)	0.066(9)	7.4
f ₅	2797.018(7)	357.5236(9)	0.054(9)	6.1
f ₆	2798.413(9)	357.3454(12)	0.041(9)	4.6
f ₇	3660.781(8)	273.1658(6)	0.049(9)	5.5
f ₈	3661.141(6)	273.13886(46)	0.061(9)	6.9
f ₉	3674.845(8)	272.1203(6)	0.046(9)	5.1
f ₁₀	3678.276(7)	271.86649(49)	0.059(10)	6.7
f ₁₁	3678.394(6)	271.85779(42)	0.068(10)	7.7

Table 3. continued.

ID	Frequency [μHz]	Period [sec]	Amplitude [ppt]	S/N
f ₁₂	3678.593(6)	271.84307(42)	0.067(10)	7.6
f ₁₃	3680.469(7)	271.7045(5)	0.056(10)	6.3
f ₁₄	3680.617(7)	271.69360(50)	0.058(10)	6.5
TIC 471015194				
f ₁	5629.2847(16)	177.64246(5)	1.22(20)	5.2
f ₂	5641.0876(10)	177.270779(33)	1.90(20)	8.1
f ₃	5788.6736(6)	172.751148(18)	3.31(20)	14.0
f ₄	6025.1463(12)	165.971073(34)	1.62(20)	6.9
f ₅	6032.7508(7)	165.761862(18)	3.02(20)	12.8

TIC 4632676 (Ton 74) is a new sdOB pulsator. The star was classified as an sdB star in the Palomar-Green (PG) survey (Green et al. 1986). Then, the star was found to be a binary system consisting of sdB and dM stars by Luo et al. (2016). Recently it was reclassified as an sdOB star by Lei et al. (2019a). TESS observed the star during Sector 49. We detected two frequencies, one in the very low frequency region, which can be interpreted as a binary frequency (orbital period of 2.619(15) days), and one in the high frequency region that we associate with a p-mode. We show the amplitude spectrum in Fig. 2, and list the prewhitened frequencies in Table 3.

TIC 26291471 (HE 1450-0957) is a known sdOB pulsator. Lisker et al. (2005) derived its atmospheric parameters indicative of an sdOB type and Østensen et al. (2010a) detected two high frequency signals. TESS observed the star during Sector 51. We detected only one frequency in the high frequency region that we associated with a p-mode. It is close but does not overlap with frequency f_1 reported by Østensen et al. (2010a). We show the amplitude spectrum in Fig. 2, and list the prewhitened frequency in Table 3.

TIC 55753808 (PG 1203+574) is a new sdOB pulsator. The star was originally classified as an sdB by Green et al. (1986). Lei et al. (2019b) derived spectroscopic parameters and classified the star as an sdOB. TESS observed the star during Sectors 41 and 48. These two data sets are many sectors apart and we decided not to merge both sets, but to analyze them separately. We detect the same single p-mode frequency in each data set. The amplitude spectra also show low frequencies, which are characteristic of binary frequencies. Our contamination analysis revealed that the binary signal comes from neighboring TIC 55753802, which is a known binary star and we provide no further analysis of this signal. We show the amplitude spectrum for Sector 41 data in Fig. 2, and list the prewhitened frequency in Table 3.

TIC 56863037 (DTLyn) is a known sdB pulsator. The star was originally classified as an sdB-O by Green et al. (1986). Koen et al. (1999) obtained photometry and a spectrum, which allowed them to sharpen the classification to sdB, and detect three p-modes. Randall et al. (2007) independently classified the star as an sdB and reported seven p-modes. They performed an asteroseismic analysis and delivered structural parameters of the star, e.g. $\log M_{\text{env}}/M_* = -4.69 \pm 0.07$, $M_* = 0.39 \pm 0.01 M_{\odot}$, $R/R_{\odot} = 0.133 \pm 0.001$. TESS observed the star during Sector 47. We detected five frequencies out of which four were previously reported by Randall et al. (2007). Frequency f_3 was not detected before, however we measured it at $S/N < 5$ so it is only a tentative detection. We show the amplitude spectrum calculated from all data in Fig. 2, and we list the prewhitened frequencies in Table 3.

TIC 60985176 (BI Ari) is a known sdOB pulsator. It was originally classified as an sdB-O by Green et al. (1986). Koen et al. (2004) constrained the classification to sdB with a G0V–G2V companion and reported a discovery of one p-mode with a period near 164 s. Reed et al. (2006) confirmed this period and detected another five. Our fit to a spectrum taken with the NOT in 2022 gives $T_{\text{eff}} = 35\,488(272)$ K, $\log(g/\text{cm s}^{-2}) = 5.49(5)$ and $\log(n(\text{He})/n(\text{H})) = -1.74(9)$, and we classified the star as an sdOB. We did the fit assuming the object is a single star. TESS observed the star during Sectors 42 and 43 and we detected three

frequencies, the same one as reported by Koen et al. (2004) and later by Reed et al. (2006), which continues to be the highest-amplitude pulsation in this star. The other two frequencies should be considered tentative. Our f_2 (8353.72 μHz) is 8.37 μHz away from Reed et al. (2006)'s f_2 (8362.09 μHz) and our very high-frequency f_3 (15350.16 μHz) is near-to twice Reed et al. (2006)'s f_3 if the latter is off by a daily alias, which could be expected from single-site ground-based data. While Reed et al. (2006) also used 20 s integrations, they did not investigate past 10 000 μHz . We show the amplitude spectrum in Fig. 2, and list the prewhitened frequencies in Table 3.

TIC 63168679 (*Gaia* DR3 675213084211549696) is a new sdOB pulsator. The star was classified as an sdOB by Lei et al. (2020). TESS observed the star during Sectors 44 and 46 from which we detected 10 frequencies. We show the amplitude spectrum in Fig. 2, and list the prewhitened frequencies in Table 3. We detect possible multiplets around 6660 and 7340 μHz . The frequency spacing between f_1 and f_3 is comparable to the one between f_7 and f_8 . However, f_2 is not located equidistant from f_1 and f_3 . If this is a triplet it is very asymmetric. Higher frequency resolution is required to make a definite statement whether these are multiplets but if confirmed, the rotation period would be around 10.5 days.

TIC 68495594 (HD 265435) is a known sdOB pulsator. This star has been extensively studied prior to our analysis by Pelisoli et al. (2021) and Jayaraman et al. (2022). Our fit to a spectrum taken with the NOT in 2018 gives $T_{\text{eff}} = 33\,253(137)$ K, $\log(g/\text{cm s}^{-2}) = 5.45(2)$ and $\log(n(\text{He})/n(\text{H})) = -1.40(5)$; the exposure time of 150 seconds is short compared to the 1.65 hr orbital period, implying minimal effects of orbital line broadening. TESS observed the star during Sectors 44, 45 and 60. The latter authors analyzed only the first two sectors mentioned, while data collected during Sector 60 were not analyzed by them. We show an amplitude spectrum for that sector in Fig. 2. It does not vary from the previous sectors significantly and we decided not to present any solution in Table 3. Since the star shows tidally tilted pulsations we expect some modes can come and go with time, however the overall picture will not change. Sector 60's data set can surely be a useful check on the model presented by Jayaraman et al. (2022), however that is beyond the scope of this paper.

TIC 82359147 (PG 1657+416) is a known sdB pulsator. It was classified as an sdB star by Green et al. (1986). Oreiro et al. (2007) confirmed the spectral classification, detected a signature of a G5 companion, and discovered high frequency signals. TESS observed the star during Sectors 51 and 52. We detected two frequencies, both previously reported by Oreiro et al. (2007). We show the amplitude spectrum in Fig. A.2, and list the prewhitened frequencies in Table 3.

TIC 88484868 (FBS 0658+627) is a new sdB pulsator. Németh et al. (2012) classified the star as an sdB. TESS observed it during Sectors 47 and 60. Since these two sectors are too far apart in time, we decided not to merge data for a Fourier analysis. We detected 12 and 17 frequencies, in both the g- and p-mode regions, in Sector 47 and 60, respectively. Although the p-mode frequencies are amplitude dominant, we detected more frequencies in the g-mode region. While the amplitudes change between sectors, most of the frequencies are detected in both sectors. f_1 –

f_0 from Sector 47 are recovered in Sector 60, but surprisingly, the frequencies of the highest-amplitude three near $2745\mu\text{Hz}$ are different with the dominant amplitude nearly doubling in Sector 60. These three frequencies may also be a rotationally split triplet, but the frequency splitting is not symmetric and it changes between sectors, making this interpretation less likely. We show the amplitude spectrum for Sector 60 data in Fig. A.2, and list the prewhitened frequencies in Table 3.

TIC 88565376 (DW Lyn) is a known sdB pulsator. It was classified as an sdB, based on spectroscopic parameters derivation, by Dreizler et al. (2002). The authors detected periodic flux variations and interpreted them by stellar pulsations. The pulsation periods were estimated around 363 and 382 s. Later, Schuh et al. (2006) collected additional data and confirmed the two periods reported by Dreizler et al. (2002) and discovered a new one in the g-mode region. The authors explained this newly detected signal as stellar pulsation, making it the first known hybrid sdBV star. TESS observed the star during Sectors 47 and 60. We only detect the two p-mode frequencies reported in previous papers. We show the amplitude spectrum calculated from Sector 47 data in Fig. A.2, and we list the prewhitened frequencies in Table 3. We did not detect the low frequency signal, although if its amplitude remained fairly constant over time, it would be clearly detected in our analysis. In fact, the p-mode amplitudes of Sector 60 are nearly the same as reported by Schuh et al. (2006) for 2004 data. Therefore, we might expect the g-mode amplitude to be roughly preserved, though it appears it has not.

TIC 90960668 (V585 Peg, Balloon 090100001) is a known sdB pulsator. This star has been extensively studied prior to our analysis by Oreiro et al. (2004); Baran et al. (2009); Telting & Østensen (2006); Van Grootel et al. (2008b) and others. TESS observed the star during Sector 56. These data are published by Reed et al. (2023) and hence we only show the amplitude spectrum in Fig. A.2 and refer readers to the latter paper for details on results of TESS data.

TIC 114196505 (*Gaia* DR3 4187241720861658624) is a new sdB pulsator. Our fit to a spectrum taken with the NOT in 2022 gives $T_{\text{eff}} = 27\,594(442)\text{ K}$, $\log(g/\text{cm s}^{-2}) = 5.30(6)$ and $\log(n(\text{He})/n(\text{H})) = -2.99(19)$, and we classified the star as an sdB. TESS observed the star during Sector 54. We detect two frequencies, which we list in Table 3 and show the amplitude spectrum in Fig. A.2. The frequency in the g-mode region has low S/N and should be confirmed.

TIC 136975077 (V2203 Cyg) is a known sdB pulsator. It was classified as an sdB by Downes (1986). Billères et al. (1998) derived an independent estimate of spectroscopic parameters and confirmed the sdB type and detected five pulsation frequencies in photometry. Koen (1998a) re-observed the star and increased the number of detected frequencies to seven. Jeffery & Pollacco (2000) used spectroscopic data to measure radial velocities of pulsations and detected two frequencies that were previously reported from both photometric analyses. Zhou et al. (2006) analyzed multi-site photometric data and detected six out of seven frequencies reported by Koen (1998a). The missing one was the lowest amplitude frequency in Koen (1998a)'s analysis. TESS observed the star during Sectors 55 and 56. We detected seven frequencies. We show the amplitude spectrum in Fig. A.2, and

we list the prewhitened frequencies in Table 3. Comparing our detection with the one presented by Koen (1998a), there is a difference in detecting close frequencies. Koen (1998a) found two close frequencies at $5413\mu\text{Hz}$, while we found only one in that region. On the other hand we found an additional frequency close to the highest amplitude one, f_2 and f_1 , respectively. We stress, however, that the frequency spacing between these two peaks is comparable to the resolution, so f_2 may just be a residual signal caused by unstable frequency/amplitude of f_1 . Our detection of seven frequencies with an amplitude order very similar to that reported more than 20 years ago, means that the pulsation mechanism remained stable in this star.

TIC 137502282 (FBS 0844+792) is a new sdOB pulsator. Our fit to a spectrum taken with the INT in 2019 gives $T_{\text{eff}} = 34\,259(267)\text{ K}$, $\log(g/\text{cm s}^{-2}) = 5.79(5)$ and $\log(n(\text{He})/n(\text{H})) = -1.31(7)$, indicating an sdOB classification. TESS observed the star during Sectors 40, 47, 53 and 60. We detect the same two frequencies of comparable amplitudes in all sectors. While the frequencies remain significant in all four sectors, the amplitude varies significantly i.e. 2.1, 3.01, 1.47 and 3.59 ppt, 3.76, 3.32, 3.66 and 3.91 ppt, for Sectors, 40, 47, 53, 60 and the lower and higher frequencies, respectively. Since merging all data together leads to a complex window function without detecting additional pulsations, we only present results from Sector 60 data analysis. We show the amplitude spectrum in Fig. A.2, and list the prewhitened frequencies in Table 3.

TIC 138618727 (KL UMa, Feige 48) is a known and well-studied sdB pulsator. Graham (1970) was the first who classified it as an sdB star. Spectroscopic estimates were reported by Koen et al. (1998b) who confirmed an sdB type, and discovered five frequencies associated with short-period pulsations modes. Reed et al. (2004) collected multi-site and multi-year photometry and reported five frequencies although some were daily aliases away from those reported by Koen et al. (1998b). Reed et al. (2004) presumed three of the frequencies formed an asymmetric triplet and predicted a rotation period which was subsequently found to match a binary period with a white dwarf companion discovered by O'Toole et al. (2004). Reed et al. (2004) also examined pulsation stability, deriving an upper limit evolutionary scale of $\dot{P}/P = 4.9 \pm 5.3 \times 17^{-16} \text{ s}^{-1}$. Charpinet et al. (2005a) reported four frequencies and their results of period fitting, which provided physical parameters of the star, e.g. $\log M_{\text{env}}/M_* = -2.97 \pm 0.09$, $M_* = 0.460 \pm 0.008 M_{\odot}$, $R/R_{\odot} = 0.2147 \pm 0.0034$. Van Grootel et al. (2008a) tested a spin-orbit synchronism and concluded that KL UMa rotates as a solid body in a tidally locked system. Subsequently, Reed et al. (2012) obtained time-resolved spectroscopy and additional photometry, which slightly shortened the binary period to 0.342(8) d, making the rotation (0.418 d) slightly subsynchronous. TESS observed the star in Sectors 41 and 48. The amplitude spectra in each sector do not contain the exactly the same signal and we decided not to merge data from both sectors. We show the amplitude spectrum for Sector 41 data in Fig. A.3, and list the prewhitened frequencies in Table 3. We detect two low-frequency signals, which we interpret as a binary frequency and its harmonic. With TESS's precision, the orbital solution derived from combined two sectors becomes 0.3436074(8) d in agreement with the Reed et al. (2012) value. These signals are the first detection of the binary signal in photometric data. In addition, we detected seven and six high-frequency signals, in Sector 41 and 48, respectively.

Frequency f_3 detected in the former data set is not significant in the latter one. Frequency 2877.16 μHz seems to be accompanied by two low amplitude sidelobe frequencies, one on each side. The frequency spacing is not equal on both sides so it does not call for a rotationally split modes, although the lower-frequency signal is spaced twice as much as the higher-frequency signal. It is still possible the three frequencies are part of a quintuplet with a frequency splitting of 1.5 μHz . This would lead to a rotation period of 7.7 d, which is not consistent with previous conclusions.

TIC 142398823 (PG 1315+645) is a new sdOB pulsator. It was classified as an sdOB+MS by Geier et al. (2017). TESS observed the star during Sectors 41, 48 and 49. The window function of the combined data is very complex, which prohibits a unique frequency selection for prewhitening. Therefore, we decided to use only combined Sectors 48 and 49 and we detected two frequencies. We show the amplitude spectrum in Fig. A.3, and list the prewhitened frequencies in Table 3.

TIC 159644241 (KIC 10139564) is a known sdB pulsator. It was classified as an sdB star by Østensen et al. (2010b) and extensively observed during the *Kepler* mission. Those data were extensively studied (Kawaler et al. 2010; Baran et al. 2012; Baran & Østensen 2013; Zong et al. 2016), making it probably the best-solved p-mode sdBV star and we refer readers to those papers which contain substantial analyses. TESS observed the star during Sectors 40, 41, 54 and 55. We detected three frequencies, two in the previously identified triplet, i.e. f_{33} and f_{35} listed by Baran et al. (2012) and one identified as a singlet, i.e. f_{18} . We show the amplitude spectrum in Fig. A.3, and list the prewhitened frequencies in Table 3.

TIC 165312944 (KYUMa) is a known sdB pulsator. Based on spectroscopic parameters Koen et al. (1999) classified it as an sdB star. The authors also reported four pulsation periods. Charpinet et al. (2005b) detected nine frequencies, including four reported by Koen et al. (1999) and derived structural parameters of the star using asteroseismology, e.g. $\log M_{\text{env}}/M_* = -4.254 \pm 0.147$, $M_* = 0.457 \pm 0.012 M_{\odot}$, $R/R_{\odot} = 0.1397 \pm 0.0028$. Reed et al. (2009) obtained time-resolved spectroscopy, detected four previously known frequencies and low-amplitude occasional transients. They inferred temperature and gravity changes for the four main frequencies. TESS observed the star during Sectors 48 and 49. We detected nine frequencies including four main ones, originally reported by Koen et al. (1999). The amplitudes vary over time and during TESS monitoring a signal at 7490 μHz became the highest amplitude one. In fact, this signal seems to be split into three components separated slightly asymmetrically by 0.74 and 0.69 μHz . If the signal was a rotationally split mode the average rotation period would equal 16.3 d. We do not see other peaks indicative of multiplets. We show the amplitude spectrum for Sector 48 and 49 data in Fig. A.3, and list the prewhitened frequencies in Table 3.

TIC 166054500 (PG 1409+605) is a new sdB pulsator. Green et al. (1986) classified it as an sdB-O. Geier et al. (2017) derived an sdOB classification and a hint of a main sequence companion. Based on a spectrum taken with the NOT in 2022 we derived an sdB+F classification but the quality of the spectrum is not sufficient to derive a reliable spectroscopic fit. TESS observed the

star during Sectors 48 and 49. We detected only one frequency, which we list in Table 2, while we showed the amplitude spectrum in Fig. A.3.

TIC 175402069 (NY Vir, PG 1336–018) is a known sdB pulsator. The star was found to be an eclipsing binary of an HW Vir type with a pulsating sdB primary by Kilkenny et al. (1998). The authors reported 0.1 d orbital period and two short period flux variations associated with stellar pulsations. The system became a subject of very intense investigation ever since. The analysis commonly undertaken was related to eclipse timings to search for additional companions to the system, and what is more essential with respect to this paper, the asteroseismic investigation to derive structural properties of the primary. Kilkenny et al. (2003) reported a list of 28 pulsation periods detected in photometric data collected during a multi-site campaign and Reed et al. (2002) found the first evidence for tidally-tipped pulsations for an sdBV star, aligning and precessing with the companion. Charpinet et al. (2008) used the Kilkenny et al. (2003) list for an asteroseismic analysis and derived parameters of the primary sdB star, e.g. $\log M_{\text{env}}/M_* = -4.54 \pm 0.07$, $M_* = 0.459 \pm 0.005 M_{\odot}$, $R/R_{\odot} = 0.151 \pm 0.001$. TESS observed the star during Sectors 46 and 50. The data were first cleaned of the binary flux variation. The amplitude spectra calculated from both sectors are different and we decided not to merge both data sets together. We detected 11 and 12 frequencies in Sector 46 and 50, respectively. We skipped signals at an orbital frequency from the highest amplitude frequency. We considered these signals to be artifacts caused by a pulsation phase change during eclipses. Four frequencies were not reported before, i.e. f_1 , f_4 , f_8 , and f_2 , f_7 in Sector 46 and 50, respectively. Frequencies f_4 and f_7 should be confirmed with more precise data. We show the amplitude spectrum for Sector 46 data in Fig. A.3, and list the prewhitened frequencies in Table 3.

TIC 178081355 (FBS 0315+417) is a new sdOB pulsator. It was classified as an sdOB by Geier et al. (2017). TESS observed the star during Sector 58. We detected three frequencies. We show the amplitude spectrum in Fig. A.3, and list the prewhitened frequencies in Table 3.

TIC 191442416 (V429 And) is a known sdB pulsator. It was classified as an sdB star by Østensen et al. (2001a). The authors reported a detection of four pulsation periods. Reed et al. (2007a) collected new photometry and detected 14 frequencies. TESS observed the star during Sector 57. We detected two frequencies, both already reported by Reed et al. (2007a). We show the amplitude spectrum in Fig. A.4, and list the prewhitened frequencies in Table 3.

TIC 202354658 (PG 1544+601) is a new sdB pulsator. It was identified as an sdB star by Green et al. (1986). TESS observed the star during Sectors 48–51 and 58. Since Sector 58 data are several months apart from the bulk of continuous data, and this stand alone data set does not allow for detecting additional frequencies, we decided to analyze only data collected during Sectors 48–51. We detected eight frequencies. We show the amplitude spectrum for Sector 48–51 data in Fig. A.4, and list the prewhitened frequencies in Table 3. The amplitude spectrum looks quite interesting. It contains two high amplitude frequencies, f_2 and f_5 . The higher one, f_5 , is surrounded by two

nearby frequencies spaced by $0.67 \mu\text{Hz}$, on average. If this is the rotationally split triplet, the rotation period is 17.3 d. In addition, both frequencies f_2 and f_5 are surrounded by low amplitude frequencies spaced exactly by $2.09 \mu\text{Hz}$. This frequency spacing would give 5.5 d rotation period. However, we lean towards interpreting the latter period as an orbital period. We do not detect any signal at $2.09 \mu\text{Hz}$, which would confirm our hunch, so follow-up spectroscopic velocities would be required to determine if this star is a binary.

TIC 207440586 (LM Dra) is a known sdOB pulsator. It was classified as an sdB by Green et al. (1986). Our fit to a spectrum taken with the NOT in 2022 gives $T_{\text{eff}} = 34\,037(132) \text{ K}$, $\log(g/\text{cm s}^{-2}) = 5.72(3)$ and $\log(n(\text{He})/n(\text{H})) = -1.58(7)$, and we classified the star as an sdOB. Silvotti et al. (2000) reported a detection of two pulsation periods. Reed et al. (2007b) analyzed an extended coverage photometric data and reported six frequencies. TESS observed the star during Sectors 49–52 and 56. The pulsations are very unstable in this star and merging all data together makes prewhitening very challenging. We decided to analyze only Sector 56 since they are described with a significantly lower noise level and allow for detection of all signals that are present in each sector data set but with higher S/N. We detected three frequencies, all of them previously reported by Reed et al. (2007b). We show the amplitude spectrum for Sector 56 data in Fig. A.4, and list the prewhitened frequencies in Table 3.

TIC 219492314 (V1078 Her) is a known sdOB pulsator. It was classified as an sDOA by Green et al. (1986), while as an sDO by Wegner & Dupuis (1993). Lei et al. (2019a) identified the star as an sdOB. Kuassivi et al. (2005) detected one pulsation mode at the surface. TESS observed the star during Sectors 51 and 52. We detected only one frequency, which is the same one as reported by Kuassivi et al. (2005). We show the amplitude spectrum in Fig. A.4, and list the prewhitened frequencies in Table 3.

TIC 240868270 (GD 274) is a new sdOB pulsator. For a long time it was considered to be a white dwarf candidate until Lei et al. (2023) classified the star as an sdOB+F9.5VI system. TESS observed the star during Sector 58. We detect five high frequencies associated with stellar pulsations and three low frequencies likely related to the binary flux variation. The latter variation is highly non-sinusoidal and three frequencies are not linear combinations, including harmonics. We denoted them with upper case letters. We show the amplitude spectrum in Fig. A.4, and list the prewhitened frequencies in Table 3.

TIC 266013993 (PG 0048+091) is a known sdB pulsator. Koen et al. (2004) classified the star as an sdB and reported a flux variability interpreted as stellar pulsations. Reed et al. (2007b) listed 28 frequencies noting that the amplitude spectrum is very variable. PG 0048+091 was observed as part of the K2 mission (Reed et al. 2019) and we refer the reader to that paper as the most complete study. TESS observed it during Sectors 42 and 43 and we detect four frequencies with well defined profiles indicating they are amplitude/frequency stable during TESS's two month coverage. We find frequencies in the list presented by Reed et al. (2007b) within a few μHz . We show the amplitude spectrum in Fig. A.4, and list the prewhitened frequencies in Table 3.

TIC 273255412 (GALEX J201337.6+092801) is a known sdB pulsator. It was classified as an sdB and a flux variability interpreted as stellar pulsations was discovered by Østensen et al. (2011). The authors listed 16 frequencies. TESS observed the star during Sector 54. We detect 26 frequencies, however the profiles of peaks are complex, which means that the frequencies/amplitudes are not stable or there are unresolved multiplets. Compared with the list presented by Østensen et al. (2011) we confirm eight frequencies, four are within a few μHz , while another four were not detected before. Frequency f_1 was not detected before and if it is a pulsation frequency it can be associated with gravity modes, which would make the star a hybrid pulsator. We show the amplitude spectrum in Fig. A.4, and list the prewhitened frequencies in Table 3.

TIC 284692897 (V2214 Cyg, KPD 1930+2752) is a known sdB pulsator. It was classified as an sdB by Downes (1986). Billères et al. (2000) reported 44 pulsation frequencies and an ellipsoidal variation in the sdB+WD binary system. Maxted et al. (2000) concluded that the star is a good candidate for the progenitor of a Type Ia supernova of this type, which will merge on an astrophysically interesting timescale. Reed et al. (2011) analyzed multisite photometric data and reported 68 frequencies and additional 13 suspected frequencies. They also reported tidally-tipped pulsations as well as binary-phase-dependent pulsations produced by tidal forces. Our fit to a spectrum taken with the NOT in 2022 gives $T_{\text{eff}} = 34\,594(236) \text{ K}$, $\log(g/\text{cm s}^{-2}) = 5.53(5)$ and $\log(n(\text{He})/n(\text{H})) = -1.61(8)$, and we classified the star as an sdB. TESS observed the star during Sectors 40, 41 and 54. We merged and analyzed only the consecutive Sectors 40 and 41 data. We detect 14 pulsation frequencies and two related to binarity. For an ellipsoidal variable the dominant amplitude frequency is half the orbital period. All but four pulsation frequencies were reported by Reed et al. (2011). The new frequencies are f_5 , f_7 , f_{13} and f_{14} . We show the amplitude spectrum for Sectors 40 and 41 in Fig. A.5, and list the prewhitened frequencies in Table 3.

TIC 309807601 (PG 1455+501) is a new sdB pulsator. It was classified as an sdB by Green et al. (1986), while Geier et al. (2017) reported an sdB+F2 classification. TESS observed the star during Sectors 49 and 50. We detect two high frequencies. We show the amplitude spectrum in Fig. A.5, and list the prewhitened frequencies in Table 3.

TIC 310937915 (EP Psc) is a known sdOB pulsator. It was classified as an sdB by Green et al. (1986). Silvotti et al. (2002a) derived spectroscopic parameters that indicate an sdOB type and they reported the discovery of three pulsation periods. Our fit to the average of 10 spectra taken with the NOT gives $T_{\text{eff}} = 34\,465(131) \text{ K}$, $\log(g/\text{cm s}^{-2}) = 5.74(2)$ and $\log(n(\text{He})/n(\text{H})) = -1.67(5)$. TESS observed the star during Sector 42. We detected only one frequency, which was the highest amplitude one reported by Silvotti et al. (2002a). We show the amplitude spectrum in Fig. A.5, and list the prewhitened frequency in Table 3.

TIC 355754830 (GALEX J063952.0+515658) is a known sdB pulsator. It was classified as an sdB by Németh et al. (2012). Vučković et al. (2012) reported the results of an analysis of multi-site photometric data and reported a signal in both high

and low frequency regions, making it a hybrid pulsator. TESS observed the star during Sector 60. We detect 14 frequencies, four and 10, in the low and high frequency regions, respectively, confirming it as a hybrid pulsator. We stress that some of the frequencies around the highest amplitude frequency may be residuals of amplitude/phase instability and not independent frequencies. We show the amplitude spectrum in Fig. A.5, and list the prewhitened frequencies in Table 3.

TIC 357232133 (GALEX J074149.0+552451) is a new sdOB pulsator. It was classified as an sdB by Németh et al. (2012) and reclassified as an sdOB by Geier et al. (2017). TESS observed the star during Sectors 47 and 60. To avoid a complex window function we analyzed Sector 47 data only. We detect four frequencies. We show the amplitude spectrum for Sector 47 data in Fig. A.5, and list the prewhitened frequencies in Table 3.

TIC 364966239 (*Gaia* DR3 2235556213015091456) is a new sdOB pulsator. Our fit to a spectrum taken with the NOT in 2019 gives $T_{\text{eff}} = 33\,587(241)$ K, $\log(g/\text{cm s}^{-2}) = 5.70(5)$ and $\log(n(\text{He})/n(\text{H})) = -1.50(7)$, and we classified the star as an sdOB. TESS observed the star during Sectors 41, 47, 54–57 and 60. To avoid complex peak profiles and difficulties with prewhitening, we combined and analyzed Sectors 54–57 and 60. We detect four frequencies, with three of them indicating a rotationally split triplet. The average frequency splitting indicates a rotation period of 20.141(21) d. We show the amplitude spectrum for Sectors 54–57 and 60 data in Fig. A.5, and list the prewhitened frequencies in Table 3.

TIC 397595169 (V391 Peg) is a known sdB pulsator. It was found to be a pulsator and classified as an sdB by Østensen et al. (2001b). The authors reported one high frequency. Silvotti et al. (2002b) analyzed multi-site photometric data and detected five frequencies. Pulsation frequencies were used by Silvotti et al. (2007) to infer the presence of a planet orbiting the sdB star, however its presence is now uncertain (Silvotti et al. 2018). TESS observed the star during Sector 56. We detect two frequencies, which were found to be the two highest in Silvotti et al. (2002b). We show the amplitude spectrum in Fig. A.5, and list the prewhitened frequencies in Table 3.

TIC 424720852 (GALEX J193832.5+560944) is a known sdB pulsator. Holdsworth et al. (2017) derived spectroscopic parameters and classified the star as an sdB. They detected one short period and interpreted it as a stellar pulsation. TESS observed the star during Sectors 40, 41, 50, 54–57 and 60. We split all data into two subsets that we analyzed separately. The first one includes the first two sectors, while the second one contains the remaining data sectors. We detect signals in both low and high frequency regions. In the former we found one and five frequencies in the first and second subsets, respectively. In the latter we found eight frequencies in both subsets. We show the amplitude spectrum calculated from Sectors 50, 54–57 and 60, in Fig. A.6, and list the prewhitened frequencies in Table 3.

TIC 441725813 (*Gaia* DR3 1655107708129775744) is a new sdB pulsator. Our fit to a spectrum taken with the NOT in 2017 gives $T_{\text{eff}} = 27\,204(141)$ K, $\log(g/\text{cm s}^{-2}) = 5.37(2)$ and $\log(n(\text{He})/n(\text{H})) = -2.93(5)$, and we classified the star as an sdB. TESS observed the star during Sectors 40, 41, 47–52 and 55–

60. The amplitude spectrum is very rich in frequencies in the low frequency region. It makes the star a g-mode-dominated sdB pulsator. To avoid a complex window function we separated all data into three subsets to make them continuous in coverage. The most signals exist in the subset of Sectors 55–60 data. The other subsets do not show any additional signals. We are aware that merging all data together would lower the noise level in an amplitude spectrum the most, however unstable pulsation modes contribute with residuals too strongly and no extra frequencies around the dominant signals can be conveniently detected. In addition, we only prewhitened signals above 2300 μHz , which can be associated with pressure modes. Frequencies in the low frequency region need individual analysis, which is beyond the scope of this work. We detect 14 frequencies that we associated with pressure modes. The most noticeable signal appears around 2769 μHz . There are three frequencies symmetrically spaced, which we interpret as rotationally split modes, suggesting a rotation period of 17.188(18) d. We show the amplitude spectrum for Sectors 55–60 data in Fig. A.6, and list the prewhitened frequencies in Table 3.

TIC 471015194 (*Gaia* DR3 2238354611842566912) is a known sdB pulsator. Prins et al. (2019) reported a discovery of a frequency at 5789.6 μHz . Our fit to a spectrum taken with the NOT in 2017 gives $T_{\text{eff}} = 33\,150(592)$ K, $\log(g/\text{cm s}^{-2}) = 5.71(12)$ and $\log(n(\text{He})/n(\text{H})) = -2.93(44)$, and we classified the star as an sdB. TESS observed the star during Sectors 40, 41, 47, 50, 54–57 and 60 in which we detect five frequencies. The highest amplitude frequency, f_3 , overlaps with the one reported by Prins et al. (2019). We show the amplitude spectrum in Fig. A.6, and list the prewhitened frequencies in Table 3.

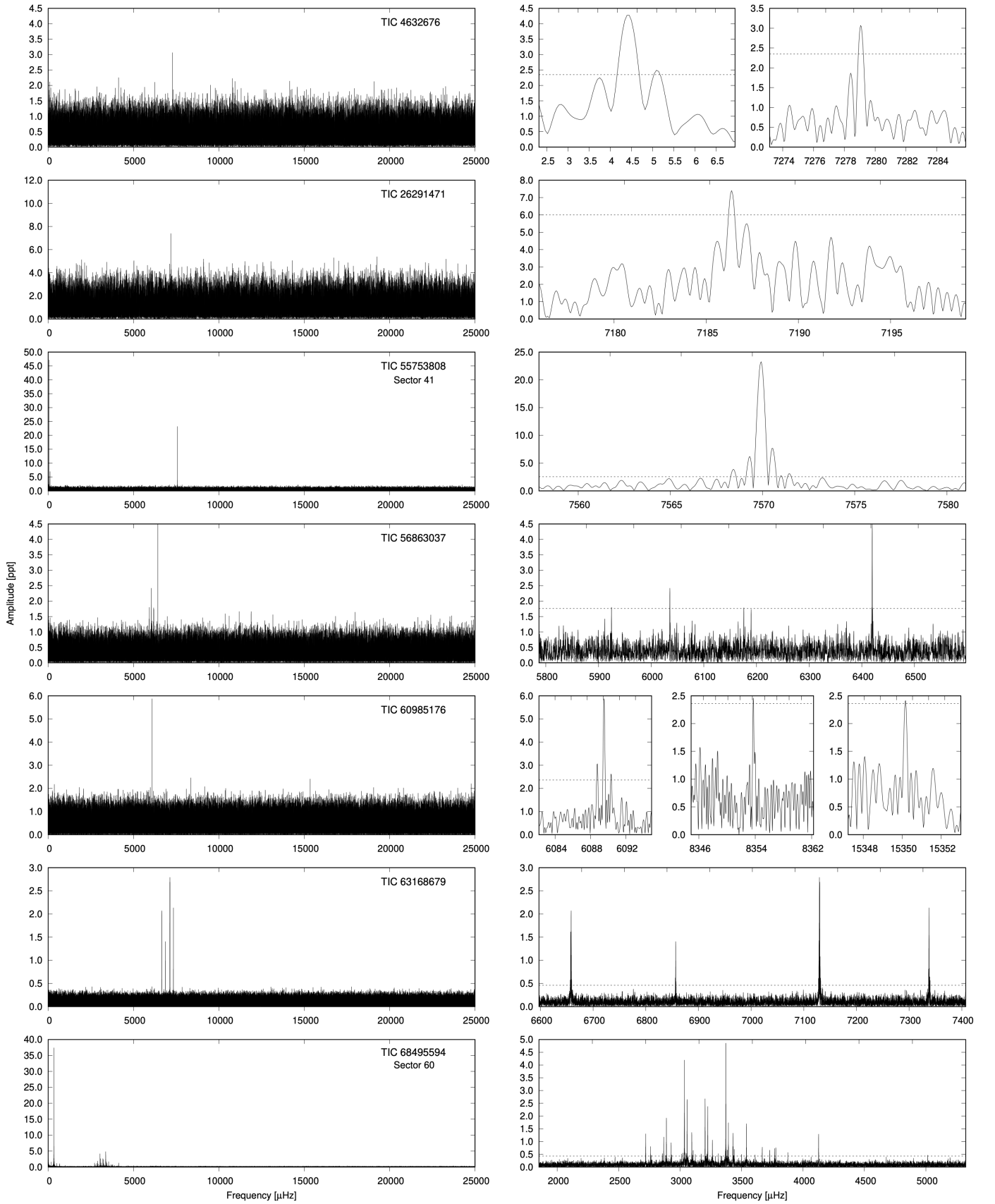


Fig. 2. Amplitude spectra of targets observed in the USC mode. If sector is not specified, we included all USC data. *Left panels:* Frequency range up to the Nyquist frequency. *Right panels:* Close-ups of the detected frequencies.

5. Discussion

In the Northern Ecliptic hemisphere we found 35 sdB and 15 sdOB p-mode pulsating stars, including 27 (18 sdB and nine sdOB) new pulsators. Overall, including the Southern Ecliptic hemisphere, with TESS data we detect p-mode pulsations in 93 hot subdwarfs, including 67 sdB, 23 sdOB, two sdO and one He-sdOB stars. Among the 48 new pulsators discovered with TESS, we identified 35 sdB, 12 sdOB and one He-sdOB stars.

5.1. Detection of pulsating hot subdwarfs with TESS

As this paper completes a TESS survey of both hemispheres, it is prudent to do a completeness study. However, such a study has many complexities, including but not limited to that TESS is a small-aperture telescope with large pixels and sdB stars tend to be on the faint end of its detection capability. Pulsation amplitudes in sdBV stars also vary substantially between stars, and often even within the same star over time (e.g. Kilkeny 2010). The highest pulsation amplitude of stars in this paper varies from under 1 to over 70 ppt, greatly affecting how bright the star would need to be to have sufficient signal-to-noise to be detected by TESS. Additionally, some stars are observed during multiple sectors, which reduces the detection threshold. To do a proper, statistically-significant determination would require an examination of all non-pulsators as well as the pulsators in this paper and likely should also include the g-mode pulsators which we exclude. Pixel decontamination from nearby stars and multi-sector normalization would also need to be completed. That analysis will be a future paper unto itself, but we will do a first-cut simplification of detection likelihood.

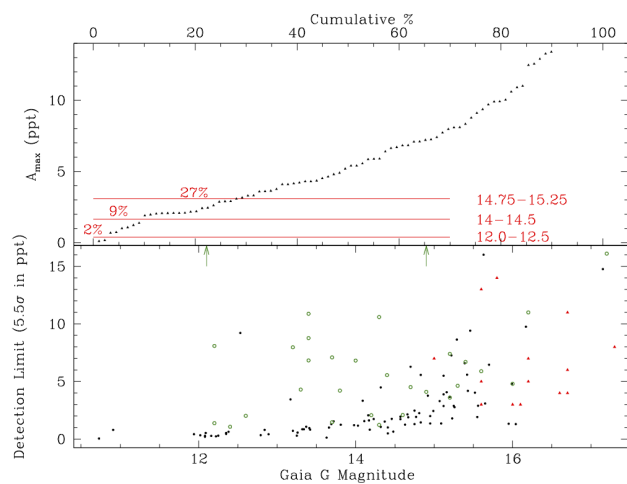


Fig. 3. Tests of detection completeness. Bottom panel: Black circles indicate single-sector detection limits of p-mode sdBV stars observed by TESS. Green circles and red triangles are not detection limits, but A_{\max} for stars listed in Østensen et al. (2010a) that were observed by TESS. The green circles indicate stars in which pulsations were detected (amplitudes from TESS data), while red triangles indicate stars in which pulsations were not detected by TESS, Østensen et al. (amplitudes as listed in 2010a). Green arrows indicate the stars TIC 90960668 and TIC 88565376, which have amplitudes too high to appear in this figure. Top panel: A_{\max} of p-mode sdBV stars (black triangles) detected by TESS from low to high amplitude. The red lines indicate detection limits for those magnitude ranges and what fraction of detected sdBV stars would be undetected based on A_{\max} .

This is done two ways. The first is to compare pulsation detection thresholds with brightness to the pulsation amplitudes actually observed by TESS. As pulsation amplitudes are brightness independent, the pulsations listed in these papers should be representative of p mode sdBV pulsations in general. By comparing the highest-amplitude pulsation for each star (A_{\max} , as only one pulsation needs to be detected to be considered a pulsator) with magnitude-averaged detection limits, we can estimate what fraction of pulsators would likely not be detected for a given magnitude. The black dots in the bottom panel of Fig. 3 are the 5.5σ detection limits for each of the TESS-observed p-mode pulsators. As expected, thresholds increase for fainter stars and beyond $G=15.25$, the scatter is quite large. We calculate average detection limits for the ranges 12-12.5 (0.385 ppt), 14-14.5 (1.65 ppt), and 14.75-15.25 (3.08 ppt) and in the top panel of Fig. 3 we compare that with A_{\max} of each TESS-observed p-mode pulsator, accumulating from lowest to highest amplitude. To keep the lower amplitudes visible, we cut off at the 90th percentile (14 ppt). Red horizontal lines indicate the average detection limit for the three brightness ranges from the bottom panel and amplitudes below those lines indicate stars which would not likely be detected as pulsators for that brightness limit. For single-sector TESS observations, the lowest-amplitude 2% of our pulsators would have been missed at magnitude 12-12.5, 9% at 14-14.5, and 27% at 14.75-15.25.

A second simple exercise is to examine a set of p-mode pulsators known previous to TESS that were observed by TESS to see if we found them as pulsators. For this exercise we used the 49 sdBV stars listed in Table 9 of Østensen et al. (2010a) of which TESS observed 45. TESS detected 30 as pulsators, with the TESS A_{\max} for those stars indicated with green open circles in the bottom panel of Fig. 3. TESS did not detect 14 stars and their A_{\max} , as listed in Østensen et al. (2010a), are indicated with red triangles. 24 of 25 (96%) stars brighter than magnitude 15.25 were detected by TESS but only 6 of 19 (32%) fainter stars were detected. The undetected star PG 1419+081, with $V=14.9$, has an A_{\max} of 7 ppt in Østensen et al. (2010a) and we find a TESS detection threshold of 3.00 ppt, so clearly it should have been detected were the pulsation amplitudes the same as in Østensen et al. (2010a).

The results from the first of these simplistic tests indicate that TESS likely missed some bright ($G<15.25$) p-mode sdB pulsators whereas the second test suggests incomplete detections only for $G>15.25$. However, the ground-based Østensen et al. (2010a) sample, which was observed for much shorter durations, all had $A_{\max} \geq 3$ ppt. This is likely a selection effect of the shorter-duration observations whereas our month-long TESS observations detect pulsators with A_{\max} as low as 1 ppt. For both tests, beyond $G=15.25$, TESS very likely misses pulsators and we would suggest that even some bright ones were missed. A more rigorous detection likelihood will be completed in an upcoming paper.

5.2. Evolutionary status and instability strip

Fig. 4 shows the distribution, in the $\log g - T_{\text{eff}}$ plane, of p-mode and hybrid hot subdwarf pulsators monitored by TESS in both the Southern and Northern Ecliptic hemispheres. Only stars with reliable estimates of their atmospheric parameters from spectroscopy are represented (see Table 4). This sample allows us to more densely map the instability region where p-mode pulsations are found and compare with evolutionary tracks and theoretical predictions from non-adiabatic pulsation calculations.

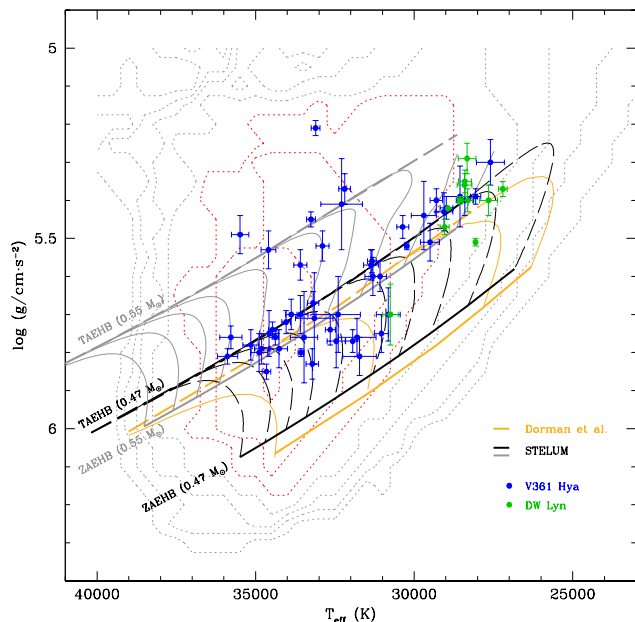


Fig. 4. Distribution, in the surface gravity ($\log g$)–effective temperature (T_{eff}) plane, of the hot subdwarf stars observed by TESS throughout cycle 1 to 4 and showing p-mode pulsations. Pure p-mode pulsators (V361 Hya stars) are represented as blue dots and hybrid pulsators featuring also g-modes (DW Lyn stars) are shown as green dots. Superimposed to this sample, the ZAEHB and TAEHB positions are indicated for an assumed core mass of $0.47 M_{\odot}$ (black curves) and $0.55 M_{\odot}$ (grey curves), illustrating how the EHB location depends on stellar mass. The models that materialize the EHB tracks are computed with the STELUM code for the specified core mass and varying envelope masses such as $D(\text{H}) \equiv \log[M_{\text{env}}/(M_{\text{core}}+M_{\text{env}})] = -6.0, -5.0, -4.5, -4.0, -3.5, -3.0, -2.75, -2.5, -2.25, -2.0$, from high to low T_{eff} . These models incorporate in their envelope nonuniform iron abundance profiles derived from equilibrium between radiative levitation and gravitational settling (see text for details). For comparison purposes, typical $0.47 M_{\odot}$ tracks assuming solar uniform envelope composition are also represented (yellow curves; Charpinet et al. 2000; Dorman et al. 1993). Dotted-line contours in the background represent the predicted number of excited $\ell = 0$ p-modes from non-adiabatic pulsation calculations as a proxy of the κ -mechanism efficiency (Charpinet et al. 2001). The three innermost contours (highlighted in red) materialize the region of the $\log g - T_{\text{eff}}$ plane where the driving of p-modes is the strongest.

In this diagram, the Zero Age and Terminal Age Extreme Horizontal Branches (ZAEHB and TAEHB) are determined from a set of static hot subdwarf models calculated with the Montréal stellar structure code STELUM (Van Grootel et al. 2013). These models span the appropriate parameter range in terms of central helium content and H-rich envelope mass to cover the entire core helium burning phase (CHeB) and the relevant part of the EHB where p-mode pulsators are located. This is unlike many diagrams of the same kind found in the literature showing tracks from standard evolutionary models. Here, we exploit the greater flexibility of static structures to illustrate various factors that may affect the position of the theoretical EHB and that are often overlooked.

A first factor is related to the actual composition of a hot subdwarf envelope which is known to be affected by microscopic diffusion, while standard evolution models usually assume a solar homogeneous composition. Diffusion has an impact on the EHB location because the sedimentation of helium and distribu-

tion of opaque elements (in particular those from the iron group) significantly change the thermal structure of the stellar envelope and consequently the surface parameters for a given envelope mass. The trend can be seen in Fig. 4 by comparing the $0.47 M_{\odot}$ tracks derived from the STELUM models, which incorporate a double layered H/He envelope with nonuniform iron-abundance distributions from calculations of equilibrium between radiative levitation and gravitational settling (see Charpinet et al. 1997 and Van Grootel et al. 2013 for details), with standard evolution models of solar composition from Dorman et al. (1993). The difference between the two is a noticeable shift of the ZAEHB and TAEHB towards lower surface gravities when microscopic diffusion is included, actually providing a better match to the distribution of observed hot subdwarf stars.

A second factor that is generally overlooked is the influence of stellar mass. Most stars that form the EHB are expected to have the canonical mass of $\sim 0.47 M_{\odot}$, corresponding to the critical value for helium ignition in degenerate conditions (the so-called helium flash), since their progenitors on the main-sequence are generally believed to be less than $2 M_{\odot}$ stars evolving through the red giant phase. This expectation is indeed mostly verified as the observed EHB appears as a rather homogeneous group that can be reasonably well reproduced, globally, with models assuming the same core mass. Nevertheless, even if the mass distribution of hot subdwarf stars is strongly peaked at the canonical value (Fontaine et al. 2012), scatter around that value is still expected that will lead to some fuzziness in the position of the ZAEHB and TAEHB. In addition, some binary evolution channels that are also invoked in the formation of hot subdwarfs – for instance, those involving the merger of two low-mass helium white dwarfs – could lead to masses significantly different from the canonical value. The existence of non-canonical massed sdB stars has indeed been suggested, either through asteroseismology (Randall et al. 2006; Fontaine et al. 2019) or from the orbital analysis of close binaries (e.g. Schaffenroth et al. 2022). In order to illustrate the impact of stellar mass on the EHB location, we also represented tracks computed with STELUM for a core mass of $0.55 M_{\odot}$ in Fig. 4. These show an important shift toward lower surface gravities and higher effective temperatures where post-EHB objects are usually expected when considering only tracks for the canonical mass. Clearly, this higher-mass EHB can no longer account for the bulk of observed sdB stars, indicating that massive hot subdwarfs must be quite rare. However, it also shows that one cannot reliably assign an evolutionary status to a given sdB star based on its position in the $\log g - T_{\text{eff}}$ plane, unless its mass is constrained through independent means. Hence, among the pulsators that are clearly above the $0.47 M_{\odot}$ TAEHB in Fig. 4, some are likely post-EHB stars, but a few may instead be core helium burning (EHB) objects with a higher mass.

The last information provided in Fig. 4 is the theoretical mapping of the p-mode instability region as predicted by the original calculations of Charpinet et al. (2001). This mapping of the $\log g - T_{\text{eff}}$ plane results from non-adiabatic pulsation calculations applied to envelope models that incorporate the same nonuniform iron profiles used in STELUM structures. It is well established that the κ -mechanism involving predominantly iron partial ionization in the Z-bump region and enhanced by radiative levitation is responsible for the driving of acoustic pulsations in V361 Hya stars (Charpinet et al. 1996; Charpinet et al. 1997). The predicted number of radial ($\ell = 0$) p-modes is used in this context as a measure of the driving efficiency. Fig. 4 shows that p-mode sdB pulsators clearly concentrate within the region where the driving is predicted to be the strongest (roughly within

Table 4. Spectroscopic estimates of pulsating hot subdwarfs reported here and in Paper I, for which we derived an acceptable spectroscopic fits. Archive spectra were (re-)fit using the same model and method as described in Section 2.

TIC	T_{eff}	σ	$\log(g/\text{cm s}^{-2})$	σ	$\log(n(\text{He})/n(\text{H}))$	σ	Telescope	Reference
968226	28 982	198	5.42	0.03	-3.15	0.09	NOT	
4632676	33 589	210	5.57	0.04	-1.64	0.05	SDSS	archive
16993518	32 194	187	5.37	0.04	-2.27	0.09	NOT	
19690565	31 033	225	5.75	0.05	-3.12	0.15	NOT	Baran et al. (2023)
26291471	34 376	106	5.76	0.02	-1.34	0.03	VLT	archive
33318760	34 806	233	5.79	0.04	-1.68	0.06	NTT	Randall et al. (2009)
47377536	35 149	251	5.78	0.04	-1.84	0.06	LAMOST	archive
55753808	34 889	263	5.80	0.05	-1.80	0.06	LAMOST	archive
56863037	31 940	220	5.77	0.03	-2.55	0.06	2.3mKP	Randall et al. (2007)
62381958	35 779	352	5.76	0.03	-1.30	0.00	NTT	archive
63168679	35 885	318	5.81	0.02	-1.60	0.03	LAMOST	archive
68495594	33 253	137	5.45	0.02	-1.40	0.05	NOT	
69298924	28 063	163	5.39	0.02	-2.97	0.06	NOT	Baran et al. (2011)
70549283	33 879	178	5.70	0.04	-1.51	0.05	LAMOST	archive
85145647	32 287	656	5.41	0.12	-3.03	0.39	INT	
88484868	29 040	140	5.47	0.02	-2.85	0.06	INT	archive
88565376	28 400	200	5.35	0.03	-2.7	0.03	3.5mCA	Dreizler et al. (2002)
90960668	28 932	23	5.421	0.003	-2.721	0.003	NOT	Østensen et al. (2007)
95752908	34 656	133	5.85	0.02	-1.31	0.03	NOT	Holdsworth et al. (2017)
114196505	27 594	442	5.30	0.06	-2.99	0.19	NOT	
136975077	31 800	600	5.76	0.05	-2.23	0.1	Keck	Heber et al. (2000)
137502282	34 259	267	5.79	0.05	-1.31	0.07	INT	
138618727	29 500	300	5.51	0.05	-2.93	0.05	Keck	Heber et al. (2000)
139481265	31 720	529	5.81	0.05	-2.23	0.08	NOT	Baran et al. (2023)
142200764	30 235	66	5.52	0.01	-2.84	0.04	VLT	archive
154818961	28 330	281	5.29	0.04	-1.71	0.05	NOT	
156618553	28 065	43	5.51	0.01	-2.45	0.02	VLT	Vučković et al. (2014)
157141133	31 076	207	5.60	0.04	-2.97	0.16	INT	
159644241	32 035	117	5.66	0.02	-2.13	0.04	NOT	Baran et al. (2012)
165312944	33 570	88	5.80	0.01	-1.47	0.03	NOT	Reed et al. (2009)
175402069	31 300	250	5.60	0.05	-2.93	0.05	VLT	Vučković et al. (2007)
178081355	33 186	176	5.67	0.03	-1.77	0.03	SDSS	archive
186484490	28 401	274	5.40	0.04	-2.90	0.09	LAMOST	archive
191442416	32 400	700	5.70	0.10	-2.20	0.20	2.2mCA	Østensen et al. (2001a)
199715319	28 144	310	5.32	0.04	-3.15	0.10	NOT	
202354658	29 060	280	5.43	0.05	-3.44	0.26	NTT/4mKP	Németh et al. (2012)
207440586	34 037	132	5.72	0.03	-1.58	0.07	NOT	
219492314	34 575	299	5.75	0.06	-1.34	0.08	LAMOST	archive
222892604	30 363	188	5.47	0.03	-3.08	0.13	NOT	
248776104	32 891	205	5.52	0.04	-2.89	0.14	NOT	
266013993	32 460	290	5.77	0.07	-2.33	0.11	NOT	Reed et al. (2009)
273255412	33 108	140	5.21	0.02	-2.63	0.07	LAMOST	archive
284692897	34 594	236	5.53	0.05	-1.61	0.08	NOT	
310937915	34 465	131	5.74	0.02	-1.67	0.05	NOT	
331656308	28 411	230	5.36	0.03	-2.95	0.11	NOT	
355754830	30 750	250	5.70	0.08	-2.59	0.29	4mKP	Vennes et al. (2011)
357232133	33 470	430	5.76	0.12	-1.93	0.17	NTT/4mKP	Németh et al. (2012)
364966239	33 587	241	5.70	0.05	-1.50	0.07	NOT	
366656123	31 331	140	5.56	0.03	-2.82	0.06	SDSS	Baran et al. (2023)
392092589	27 654	280	5.40	0.04	-2.97	0.10	NOT	
396954061	33 214	199	5.83	0.04	-1.57	0.04	NOT	
397595169	29 300	200	5.40	0.03	-3.00	0.15	3.5mCA	Østensen et al. (2001b)
424720852	28 311	149	5.40	0.03	-2.79	0.07	INT	archive
436579904	31 360	240	5.57	0.04	-2.65	0.10	NOT	Reed et al. (2020)
437043466	28 557	82	5.40	0.01	-3.07	0.02	NOT	Baran et al. (2017)
441725813	27 204	141	5.37	0.02	-2.93	0.05	NOT	
455095580	30 817	380	5.70	0.07	-2.60	0.16	NOT	Baran et al. (2023)
471013461	28 551	548	5.39	0.08	-2.94	0.02	SOAR	archive
471015194	33 150	592	5.71	0.12	-2.93	0.44	NOT	
673345538	29 693	396	5.44	0.09	-2.72	0.21	LAMOST	archive

the three innermost contours), as one would expect, thus supporting that the identification of the main processes which drive oscillations in these stars is correct. The true extent of the p-mode instability region remains uncertain, however. Predicted instabilities (all contours) derived from the assumption of equilibrium between radiative levitation and gravitational settling cover a wider region than the observed instability strip. Charpinet et al. (2009) demonstrated that the strength of the driving engine is predominantly determined by the amount of heavy metals (in particular iron) present at the Z-bump location, irrelevant of the composition in other parts of the envelope. The extent of the instability region is therefore sensitive to the precise amount of heavy metals that can accumulate in that region of the stellar envelope, which is likely modulated by various competing mixing processes that were not all included in the aforementioned calculations (e.g., stellar winds, thermohaline mixing; Théado et al. 2009; Hu et al. 2011). The fact that the observed instability strip is narrower than the predicted one indeed pleads for competing processes that slow down or reduce the efficiency of radiative levitation, the diffusive equilibrium assumption providing an upper limit for the amount of levitating heavy metals. It is also possible that other opaque elements such as nickel play a role in shaping the instability region, although Jeffery & Saio (2006a,b, 2007) showed that nickel at least had little impact on the p-mode instability strip location, unlike for the g-modes.

Overall, Fig. 4 reveals that the distribution of p-mode pulsators is compatible with the canonical $\sim 0.47 M_{\odot}$ EHB covering all stages of the core helium burning phase, from the ZAEHB to TAEHB. The eight sdB pulsators located well above the TAEHB could be either in a post-EHB, helium shell burning stage or, as discussed above, higher mass sdB stars. The numbers involved, eight versus 60 objects for the main group (i.e. a fraction of one out of eight stars) suggests that higher mass sdBs likely dominate the sample since respective evolution timescales on the EHB and post-EHB would imply a fraction closer to one out of ~ 30 . Hence, statistically speaking (with all due caution when small numbers are involved), among the eight outliers only two should be post-EHB stars and six hot subdwarfs with significantly higher masses.

Another interesting observation is the concentration of the coolest pulsators near the TAEHB, or equivalently a complete lack of them in earlier stages, closer to the ZAEHB. Considering the size of the sample, we estimate that this trend is real. It could be naturally explained by the fact that, at effective temperatures around 29 000 K, the intersection of the region of strongest driving efficiency occurs near the TAEHB and does not cover the earlier stages, contrary to the hotter regions located around 34 000 K where most V361 Hya stars are found. Interestingly, a similar trend, although less obvious, may exist for the hottest pulsators, above $\sim 34 000$ K. If that was to be confirmed, the argument of the driving efficiency as mapped in Fig. 4 would not hold. A potential culprit could then be the growing influence of stellar winds that become more proficient at higher effective temperatures and that could slow down the microscopic diffusion of elements and the onset of favorable conditions for the pulsations to develop. This being posited, we refrain from speculating further on this issue until the reality of the deficit of hot pulsators close to the ZAEHB is confirmed.

5.3. Pulsation periods vs T_{eff} and $\log g$

Charpinet et al. (2002) presented the pulsation period of p-modes as functions of T_{eff} and $\log g$. In their Fig. 9, they presented results for radial ($\ell = 0$) and non-radial ($\ell = 1, 2, 3$) modes of radial

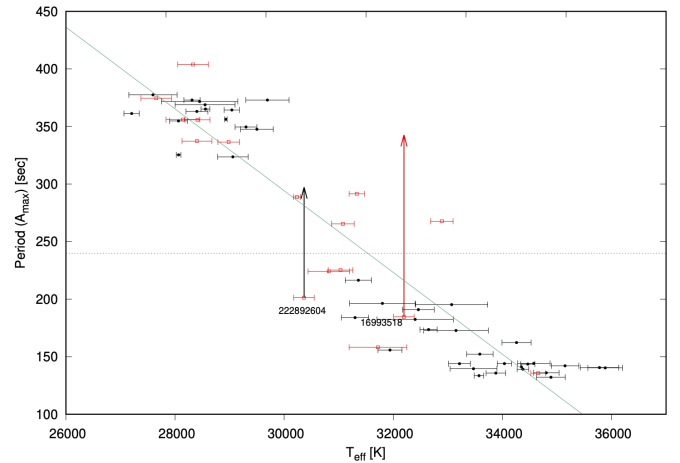


Fig. 5. Pulsation periods with the highest amplitudes in function of T_{eff} . Black dots represent USC stars, open red boxes represent SC stars, a horizontal dotted line is the Nyquist period, and the solid sloped line is a fit to the USC stars.

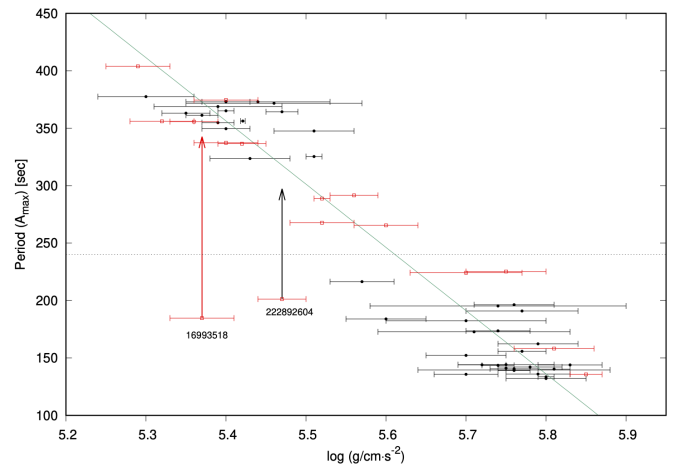


Fig. 6. Same as in Fig. 5 but in function of $\log g$.

orders $k = 0, 1$ and 10. Pulsation periods of radial modes do not depend much on T_{eff} while they are strongly and monotonically affected by $\log g$. For non-radial modes both the temperature and gravity can influence the pulsation periods. These change more rapidly with temperature for low radial order cases, and with surface gravity for higher radial order cases. Modal degree does not influence pulsation periods significantly.

Making such an observational plot would have two benefits. Firstly, for a given mode geometry, we can independently derive the effective temperature and/or surface gravity based on a pulsation period. Secondly, if both spectroscopic and period estimates are available, we can test structural models. To compare theoretical and observational counterparts we assume that the frequencies we plot represent the same modal degree and radial order, or that their differences do not significantly change the picture shown in Fig. 9 of Charpinet et al. (2002).

Observational counterpart of pulsation periods in function of T_{eff} was reported by e.g. Reed et al. (2023) who noted an observational correlation between T_{eff} and the period of the highest-amplitude pulsation (shown in their Figure 11, which was a modified version from Reed et al. (2021)). They examined both p- and g-mode hot subdwarf pulsators, though their sample was heavily dominated by the latter group. Since our work is fo-

cused on p-mode pulsators we have significantly updated this figure in the short period range and we also plotted pulsation periods as a function of $\log g$. We obtained reliable estimates of T_{eff} and $\log g$ for 41 USC and 16 SC stars, which is 61% of the p-mode pulsators reported in both Paper I and this paper. This large sample allows us to make a more detailed analysis of the relationship between the period of the highest amplitude (noted as $\text{Period}(A_{\text{max}})$ in our figures) and $T_{\text{eff}}/\log g$.

As mentioned in Section 4 we can uniquely identify the frequencies only in the USC data (except for TIC 220573709). Therefore, we used only USC stars with reliable spectroscopic estimates and plotted pulsation periods as functions of T_{eff} and $\log g$ in Figs. 5 and 6. We used pulsation periods with the highest amplitudes, which are not necessarily of the same modal degree and radial order, as presented by Charpinet et al. (2002) in their Fig. 9. According to the surface cancellation effect, it is more likely to detect low degree modes, hence we expect those highest amplitude frequencies will likely be assigned with either $\ell = 0$ or 1. The radial order remains unconstrained. Another caveat of our analysis is that the periods having the highest amplitudes can change with time. Depending on which data set is used, a pulsation period shown in Figs. 5 and 6 may not be unique. However, the range of highest-amplitude p-mode pulsation periods in a single star typically does not vary by more than 50 s for pulsations around 3500 μHz and decreases toward higher frequencies. Therefore, our selection of periods with the highest amplitudes should not significantly blur the picture in those two figures.

There are noticeable trends in both diagrams, which look more or less linear. However there is significant scatter so it may also be slightly curved/wiggled. Given the scatter in our diagrams we are not able to discern between linear and nonlinear trends plotted in Fig. 9 of Charpinet et al. (2002). We fitted lines to both data sets. Then we added SC stars to see if our sub-/super-Nyquist choices match the trends in the diagrams. The majority of SC stars go along the trend, but we found two stars in the $\log g$ diagram (Fig. 6) which do not match the fit too well. We marked them with their TIC names. Keeping in mind that our arbitrary super-Nyquist choice could not be correct, we added arrows, which indicate shifts from their super- to sub-Nyquist frequencies. The shift brings the periods of both stars significantly closer to the fit for $\log g$. However, no shift was necessary in the T_{eff} figure as these two stars in that latter figure were not outliers. In the case of TIC 222892604, the shift moved the star closer to the trend, which supports the shift in the $\log g$ diagram. The case of TIC 16993518 is different. The shift in $\log g$ moves the star away from the trend, which does not support a necessity for the shift in the T_{eff} diagram. We consider the spectroscopic determination of $\log g$ for TIC 16993518 to be reliable and since all its pulsations are within a narrow range, changing its highest-amplitude frequency would have little effect. Therefore, TIC 16993518 appears to be an outlier of the trend in the T_{eff} diagram.

6. Summary and conclusions

We presented results of our search for short-period hot subdwarf pulsators observed in Years 2 and 4 of the TESS mission. We identified 50 short-period hot-subdwarf pulsators, in addition to 43 found in Years 1 and 3 and reported by Baran et al. (2023). We presented the list of prewhitened frequencies and we made an attempt to identify possible multiplets caused by stellar rotation. We selected five candidates with rotation periods between 11 and 46 d. Our work completed the search for p-mode pulsating hot subdwarfs in TESS Sectors 1–60, and allowed us to

present a completeness study, discuss an evolutionary status and instability strips of our findings, and compare pulsation periods vs effective temperature and surface gravity with theoretical predictions. We found that the percentage of undetected pulsators in the TESS mission reaches 25% near the 15th magnitude. We underlined the importance of a proper treatment of the hydrogen-rich envelope composition (strongly affected by microscopic diffusion processes) when comparing the distribution of hot subdwarfs in the $\log g$ - T_{eff} plane with stellar models. We also emphasized that the stellar mass plays a significant role in understanding the instability strip. Based on the width of the p-mode instability strip we deduced that competing mixing processes ignored in the non-adiabatic calculations must play a role to reduce the amount of levitating iron in the stellar envelope. We found that the coolest p-mode pulsators tend to cluster around the Terminal Age of the Extreme Horizontal Branch of $\sim 0.47 M_{\odot}$. Finally, we derived pulsation period distributions that agree with the predicted trends in T_{eff} and $\log g$.

Acknowledgements. Financial support from the National Science Centre Poland under project No. UMO-2017/26/E/ST9/00703 is acknowledged. SC acknowledges financial support from the Centre National d'Études Spatiales (CNES, France) and from the Agence Nationale de la Recherche (ANR, France) under grant ANR-17-CE31-0018. PN acknowledges support from the Grant Agency of the Czech Republic (GAČR 22-34467S). The Astronomical Institute in Ondřejov is supported by the project RVO:67985815. This paper includes data collected with the TESS mission, obtained from the MAST data archive at the Space Telescope Science Institute (STScI). Funding for the TESS mission is provided by the NASA Explorer Program. STScI is operated by the Association of Universities for Research in Astronomy, Inc., under NASA contract NAS 5-26555. This paper uses observations made with the Nordic Optical Telescope, owned in collaboration by the University of Turku and Aarhus University, and operated jointly by Aarhus University, the University of Turku and the University of Oslo, representing Denmark, Finland and Norway, the University of Iceland and Stockholm University at the Observatorio del Roque de los Muchachos, La Palma, Spain, of the Instituto de Astrofísica de Canarias. This research has made use of the SIMBAD database, operated at CDS, Strasbourg, France. This paper uses observations from the 2.2m and 3.5m Calar Alto, 2.3m and 4m Kitt Peak, INT (ING), Keck, LAMOST, NTT and VLT (ESO), SOAR, and SDSS telescopes. This work has also made use of data from the European Space Agency (ESA) mission *Gaia* (<https://www.cosmos.esa.int/gaia>), processed by the *Gaia* Data Processing and Analysis Consortium (DPAC, <https://www.cosmos.esa.int/web/gaia/dpac/consortium>). Funding for the DPAC has been provided by national institutions, in particular the institutions participating in the *Gaia* Multilateral Agreement. V.V.G. is a F.R.S.-FNRS Research Associate. This research has used the services of www.Astroserver.org.

References

- Abrahamian, H. V., Lipovetski, V. A., Mickaelian, A. M., & Stepanian, J. A. 1990, *Astrofizika*, 33, 213
- Baran, A., Oreiro, R., Pigulski, A., et al. 2009, *MNRAS*, 392, 1092
- Baran, A. S., Gilker, J. T., Reed, M. D., et al. 2011, *MNRAS*, 413, 2838
- Baran, A. S. & Koen, C. 2021, *Acta Astron.*, 71, 113
- Baran, A. S. & Østensen, R. H. 2013, *Acta Astron.*, 63, 79
- Baran, A. S., Reed, M. D., Østensen, R. H., Telting, J. H., & Jeffery, C. S. 2017, *A&A*, 597, A95
- Baran, A. S., Reed, M. D., Stello, D., et al. 2012, *MNRAS*, 424, 2686
- Baran, A. S., Van Grootel, V., Østensen, R. H., et al. 2023, *A&A*, 669, A48
- Billères, M., Fontaine, G., Brassard, P., et al. 2000, *ApJ*, 530, 441
- Billères, M., Fontaine, G., Brassard, P., et al. 1998, *ApJ*, 494, L75
- Charpinet, S., Fontaine, G., & Brassard, P. 2001, *PASP*, 113, 775
- Charpinet, S., Fontaine, G., & Brassard, P. 2009, *A&A*, 493, 595
- Charpinet, S., Fontaine, G., Brassard, P., et al. 2005a, *A&A*, 443, 251
- Charpinet, S., Fontaine, G., Brassard, P., et al. 1997, *ApJ*, 483, 123
- Charpinet, S., Fontaine, G., Brassard, P., & Dorman, B. 1996, *ApJ*, 471, L103
- Charpinet, S., Fontaine, G., Brassard, P., & Dorman, B. 2000, *ApJS*, 131, 223
- Charpinet, S., Fontaine, G., Brassard, P., & Dorman, B. 2002, *ApJS*, 139, 487
- Charpinet, S., Fontaine, G., Brassard, P., Green, E. M., & Chayer, P. 2005b, *A&A*, 437, 575
- Charpinet, S., Green, E. M., Baglin, A., et al. 2010, *A&A*, 516, L6
- Charpinet, S., Van Grootel, V., Reese, D., et al. 2008, *A&A*, 489, 377
- Dorman, B., Rood, R. T., & O'Connell, R. W. 1993, *ApJ*, 419, 596
- Downes, R. A. 1986, *ApJS*, 61, 569
- Dreizler, S., Schuh, S. L., Deetjen, J. L., Edelmann, H., & Heber, U. 2002, *A&A*, 386, 249
- Fontaine, G., Bergeron, P., Brassard, P., et al. 2019, *ApJ*, 880, 79
- Fontaine, G., Brassard, P., Charpinet, S., et al. 2012, *A&A*, 539, 12
- Geier, S., Østensen, R. H., Nemeth, P., et al. 2017, *A&A*, 600, A50
- Graham, J. A. 1970, *PASP*, 82, 1305
- Green, R. F., Schmidt, M., & Liebert, J. 1986, *ApJS*, 61, 305
- Heber, U., Reid, I. N., & Werner, K. 2000, *A&A*, 363, 198
- Holdsworth, D. L., Østensen, R. H., Smalley, B., & Telting, J. H. 2017, *MNRAS*, 466, 5020
- Hu, H., Tout, C. A., Glebbeek, E., & Dupret, M. A. 2011, *MNRAS*, 418, 195
- Jayaraman, R., Handler, G., Rappaport, S. A., et al. 2022, *ApJ*, 928, L14
- Jeffery, C. S. & Pollacco, D. 2000, *MNRAS*, 318, 974
- Jeffery, C. S. & Saio, H. 2006a, *MNRAS*, 371, 659
- Jeffery, C. S. & Saio, H. 2006b, *MNRAS*, 372, L48
- Jeffery, C. S. & Saio, H. 2007, *MNRAS*, 378, 379
- Kawaler, S. D., Reed, M. D., Quint, A. C., et al. 2010, *MNRAS*, 409, 1487
- Kilkenny, D. 1984, *MNRAS*, 211, 969
- Kilkenny, D. 2010, *Ap&SS*, 329, 175
- Kilkenny, D., Heber, U., & Drilling, J. S. 1988, *South African Astronomical Observatory Circular*, 12, 1
- Kilkenny, D., O'Donoghue, D., Koen, C., Lynas-Gray, A. E., & van Wyk, F. 1998, *MNRAS*, 296, 329
- Kilkenny, D., Reed, M. D., O'Donoghue, D., et al. 2003, *MNRAS*, 345, 834
- Koen, C. 1998a, *MNRAS*, 300, 567
- Koen, C., O'Donoghue, D., Kilkenny, D., & Pollacco, D. L. 2004, *New A*, 9, 565
- Koen, C., O'Donoghue, D., Pollacco, D. L., & Charpinet, S. 1999, *MNRAS*, 305, 28
- Koen, C., O'Donoghue, D., Pollacco, D. L., & Nitta, A. 1998b, *MNRAS*, 300, 1105
- Kuassivi, Bonanno, A., & Ferlet, R. 2005, *A&A*, 442, 1015
- Lei, Z., Bu, Y., Zhao, J., Németh, P., & Zhao, G. 2019b, *PASJ*, 71, 41
- Lei, Z., He, R., Németh, P., et al. 2023, *ApJ*, 942, 109
- Lei, Z., Zhao, J., Németh, P., & Zhao, G. 2019a, *ApJ*, 881, 135
- Lei, Z., Zhao, J., Németh, P., & Zhao, G. 2020, *ApJ*, 889, 117
- Lisker, T., Heber, U., Napiwotzki, R., et al. 2005, *A&A*, 430, 223
- Luo, Y.-P., Németh, P., Liu, C., Deng, L.-C., & Han, Z.-W. 2016, *ApJ*, 818, 202
- Maxted, P. F. L., Marsh, T. R., & North, R. C. 2000, *MNRAS*, 317, L41
- Nassau, J. J. & Stephenson, C. B. 1963, *Hamburger Sternw. Warner & Swasey Obs.*, C04, 0
- Németh, P., Kawka, A., & Vennes, S. 2012, *MNRAS*, 427, 2180
- Oreiro, R., Pérez Hernández, F., Østensen, R., et al. 2007, *A&A*, 461, 585
- Oreiro, R., Ulla, A., Pérez Hernández, F., et al. 2004, *A&A*, 418, 243
- Østensen, R., Heber, U., Silvotti, R., et al. 2001a, *A&A*, 378, 466
- Østensen, R., Solheim, J. E., Heber, U., et al. 2001b, *A&A*, 368, 175
- Østensen, R., Telting, J., & Heber, U. 2007, *Communications in Asteroseismology*, 150, 265
- Østensen, R. H., Geier, S., Schaffenroth, V., et al. 2013, *A&A*, 559, A35
- Østensen, R. H., Oreiro, R., Solheim, J. E., et al. 2010a, *A&A*, 513, A6
- Østensen, R. H., Pápics, P. I., Oreiro, R., et al. 2011, *ApJ*, 731, L13
- Østensen, R. H., Silvotti, R., Charpinet, S., et al. 2010b, *MNRAS*, 409, 1470
- O'Toole, S. J., Heber, U., & Benjamin, R. A. 2004, *A&A*, 422, 1053
- Pelisolli, I., Neunteufel, P., Geier, S., et al. 2021, *Nature Astronomy*, 5, 1052

- Pérez-Fernández, E., Ulla, A., Solano, E., Oreiro, R., & Rodrigo, C. 2016, *MNRAS*, 457, 3396
- Prins, S., Telting, J., & Østensen, R. 2019, *Open Astronomy*, 28, 61
- Randall, S. K., Fontaine, G., Charpinet, S., et al. 2006, *ApJ*, 648, 637
- Randall, S. K., Green, E. M., Van Grootel, V., et al. 2007, *A&A*, 476, 1317
- Randall, S. K., Van Grootel, V., Fontaine, G., Charpinet, S., & Brassard, P. 2009, *A&A*, 507, 911
- Reed, M. D., Baran, A. S., Telting, J. H., & Østensen, R. H. 2023, *MNRAS*, 525, 1342
- Reed, M. D., Eggen, J. R., Harms, S. L., et al. 2009, *A&A*, 493, 175
- Reed, M. D., Eggen, J. R., Zhou, A. Y., et al. 2006, *MNRAS*, 369, 1529
- Reed, M. D., Harms, S. L., Poindexter, S., et al. 2011, *MNRAS*, 412, 371
- Reed, M. D., Kawaler, S. D., Zola, S., et al. 2004, *MNRAS*, 348, 1164
- Reed, M. D., O’Toole, S. J., Telting, J. H., et al. 2012, in *Astronomical Society of the Pacific Conference Series*, Vol. 452, *Fifth Meeting on Hot Subdwarf Stars and Related Objects*, ed. D. Kilkenney, C. S. Jeffery, & C. Koen, 193
- Reed, M. D., O’Toole, S. J., Terndrup, D. M., et al. 2007b, *ApJ*, 664, 518
- Reed, M. D., Slayton, A., Baran, A. S., et al. 2021, *MNRAS*, 507, 4178
- Reed, M. D., Telting, J. H., Ketzner, L., et al. 2019, *MNRAS*, 483, 2282
- Reed, M. D., Terndrup, D. M., Zhou, A. Y., et al. 2007a, *MNRAS*, 378, 1049
- Reed, M. D., Whole Earth Telescope Xcov 17 Team, & Whole Earth Telescope Xcov 21 Team. 2002, in *Astronomical Society of the Pacific Conference Series*, Vol. 259, *IAU Colloq. 185: Radial and Nonradial Pulsations as Probes of Stellar Physics*, ed. C. Aerts, T. R. Bedding, & J. Christensen-Dalsgaard, 368
- Reed, M. D., Yeager, M., Vos, J., et al. 2020, *MNRAS*, 492, 5202
- Schafferoth, V., Pelisoli, I., Barlow, B. N., Geier, S., & Kupfer, T. 2022, *A&A*, 666, A182
- Schuh, S., Huber, J., Dreizler, S., et al. 2006, *A&A*, 445, L31
- Silvotti, R., Janulis, R., Schuh, S. L., et al. 2002b, *A&A*, 389, 180
- Silvotti, R., Østensen, R., Heber, U., et al. 2002a, *A&A*, 383, 239
- Silvotti, R., Schuh, S., Janulis, R., et al. 2007, *Nature*, 449, 189
- Silvotti, R., Schuh, S., Kim, S. L., et al. 2018, *A&A*, 611, A85
- Silvotti, R., Solheim, J. E., Gonzalez Perez, J. M., et al. 2000, *A&A*, 359, 1068
- Telting, J. H. & Østensen, R. H. 2006, *A&A*, 450, 1149
- Théado, S., Vauclair, S., Alecian, G., & LeBlanc, F. 2009, *ApJ*, 704, 1262
- Van Grootel, V., Charpinet, S., Brassard, P., Fontaine, G., & Green, E. M. 2013, *A&A*, 553, A97
- Van Grootel, V., Charpinet, S., Fontaine, G., & Brassard, P. 2008a, *A&A*, 483, 875
- Van Grootel, V., Charpinet, S., Fontaine, G., et al. 2008b, *A&A*, 488, 685
- Vennes, S., Kawka, A., & Németh, P. 2011, *MNRAS*, 410, 2095
- Vučković, M., Aerts, C., Østensen, R., et al. 2007, *A&A*, 471, 605
- Vučković, M., Bloemen, S., & Østensen, R. 2014, in *Astronomical Society of the Pacific Conference Series*, Vol. 481, *6th Meeting on Hot Subdwarf Stars and Related Objects*, ed. V. van Grootel, E. Green, G. Fontaine, & S. Charpinet, 259
- Vučković, M., Østensen, R. H., Acke, B., et al. 2012, in *Astronomical Society of the Pacific Conference Series*, Vol. 452, *Fifth Meeting on Hot Subdwarf Stars and Related Objects*, ed. D. Kilkenney, C. S. Jeffery, & C. Koen, 257
- Wegner, G. & Dupuis, J. 1993, *AJ*, 106, 390
- Zhou, A. Y., Reed, M. D., Harms, S., et al. 2006, *MNRAS*, 367, 179
- Zong, W., Charpinet, S., & Vauclair, G. 2016, *A&A*, 594, A46

Appendix A: Additional figures

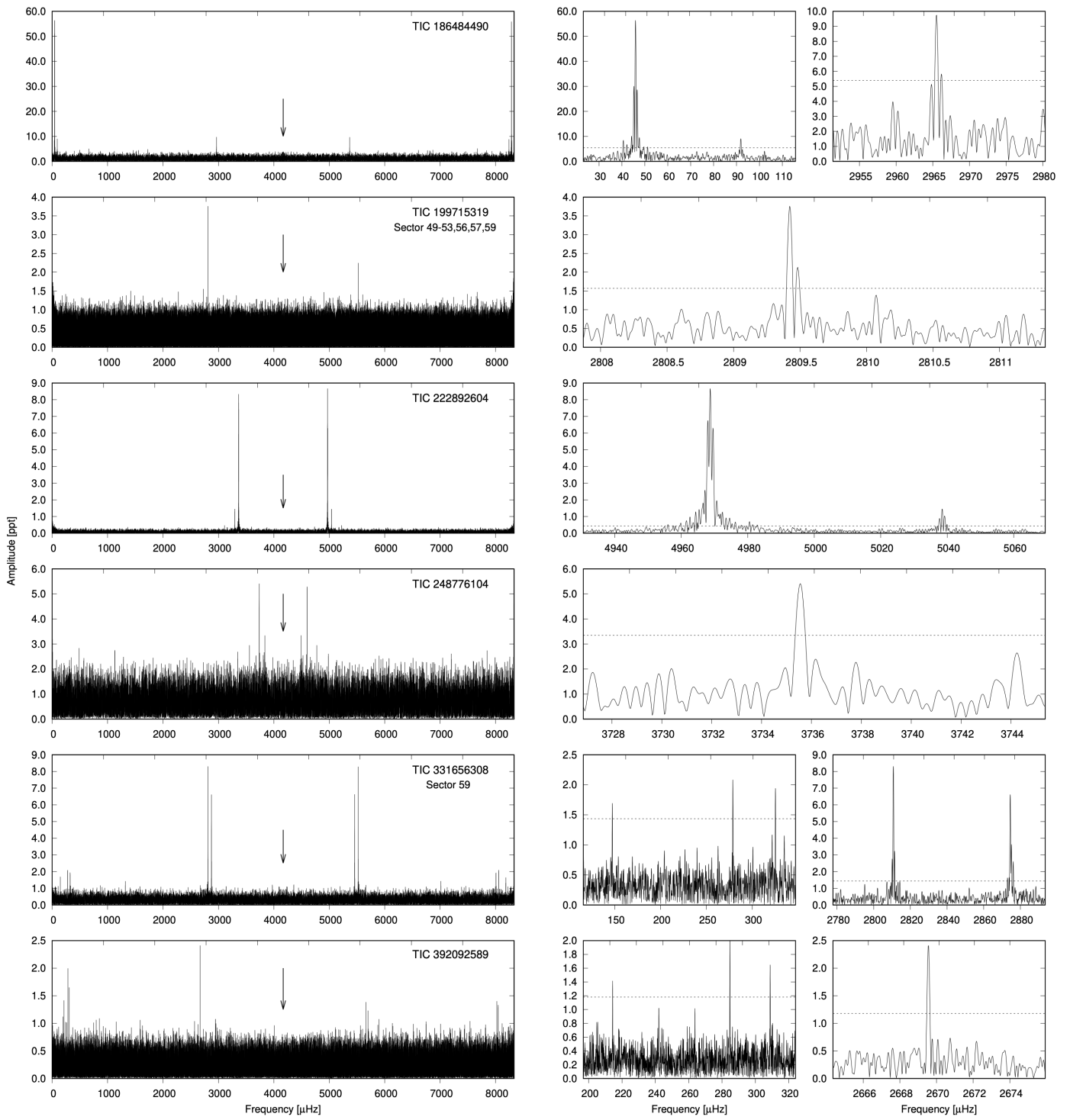


Fig. A.1. Same as in Fig. 1, but for another six targets observed only in the SC mode.

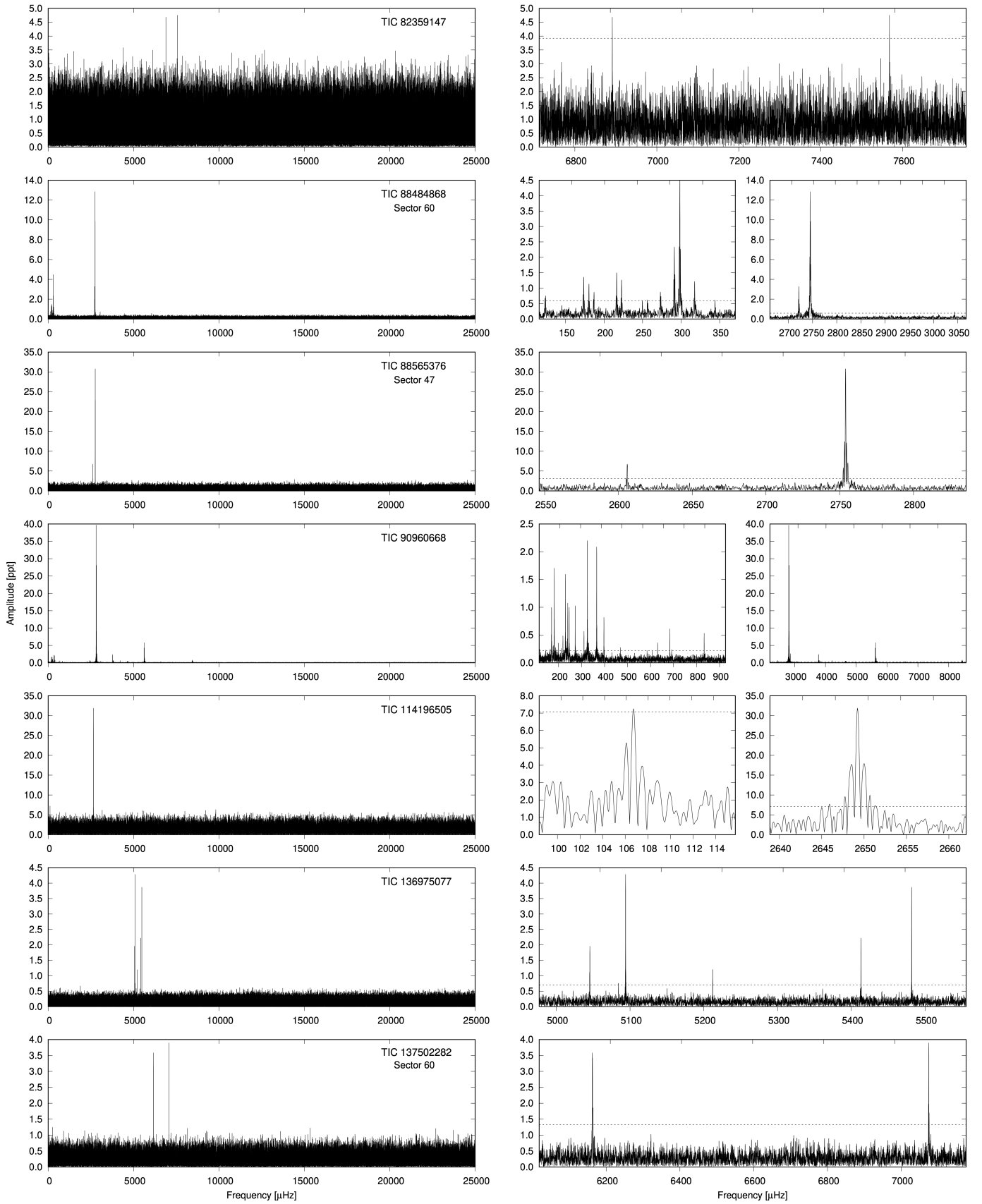


Fig. A.2. Same as in Fig. 2, but for another seven targets observed in the USC mode.

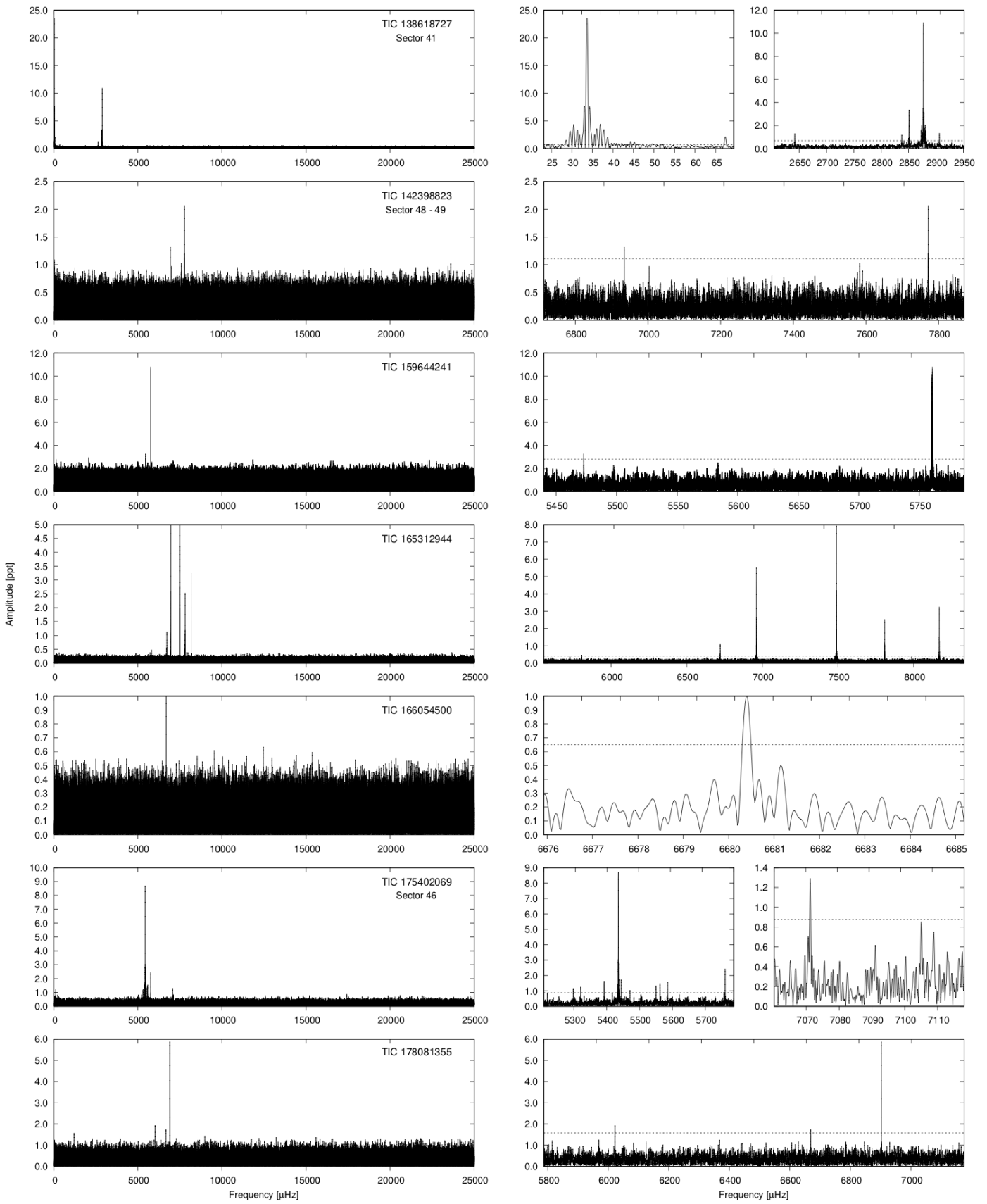


Fig. A.3. Same as in Fig. 2 but for another seven targets observed in the USC.

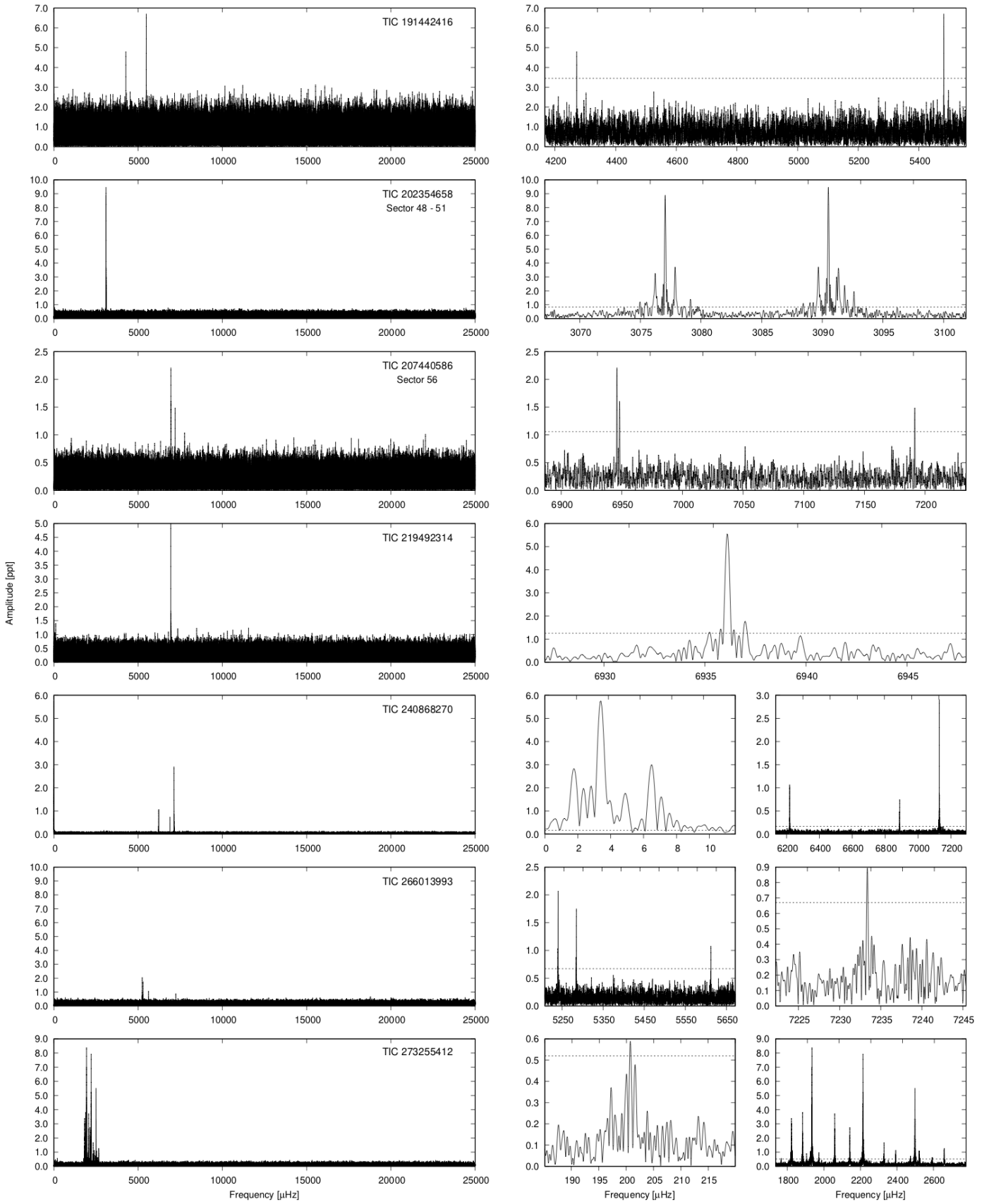


Fig. A.4. Same as in Fig. 2, but for another seven targets observed in the USC mode.

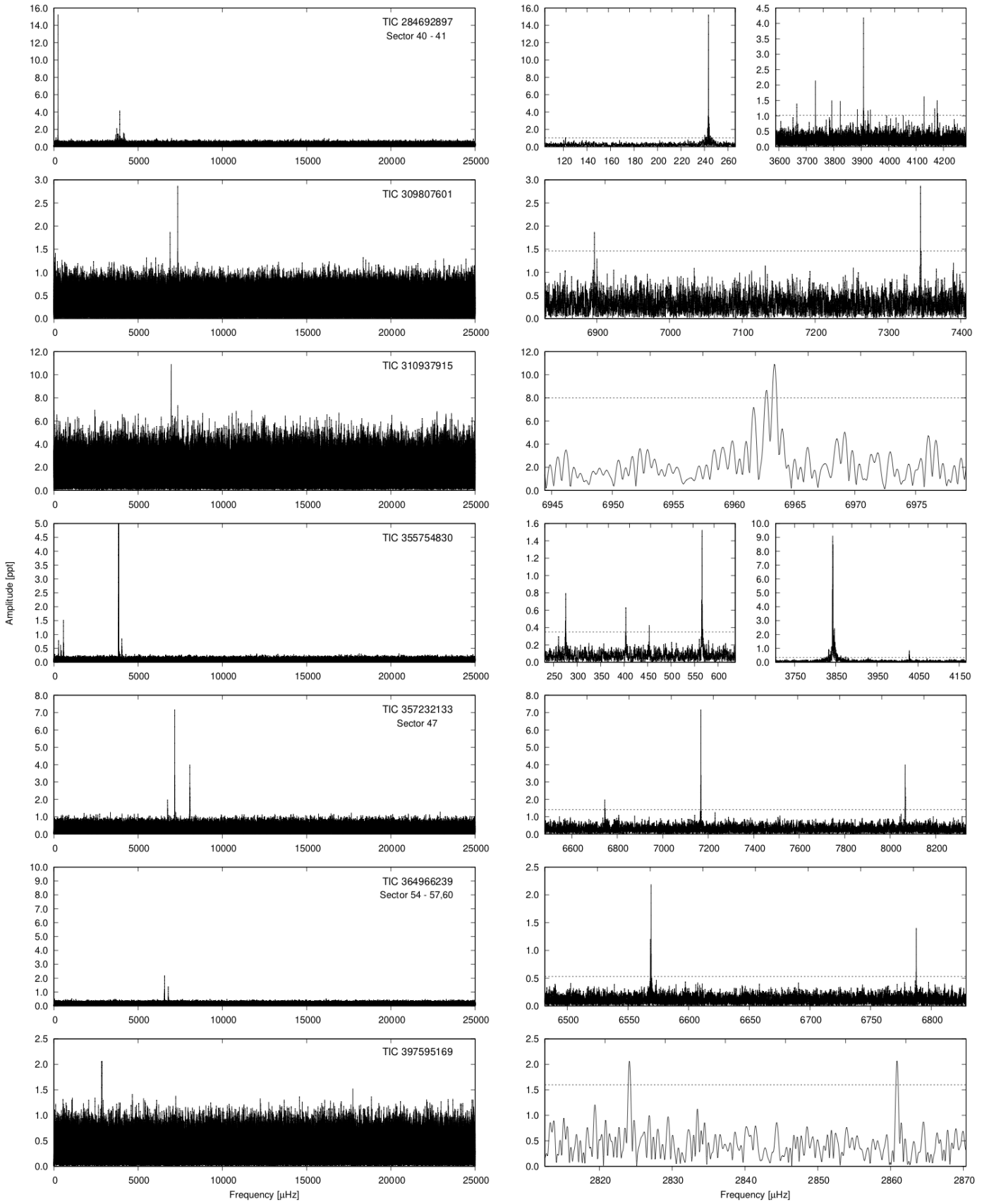


Fig. A.5. Same as in Fig. 2, but for another seven targets observed in the USC mode.

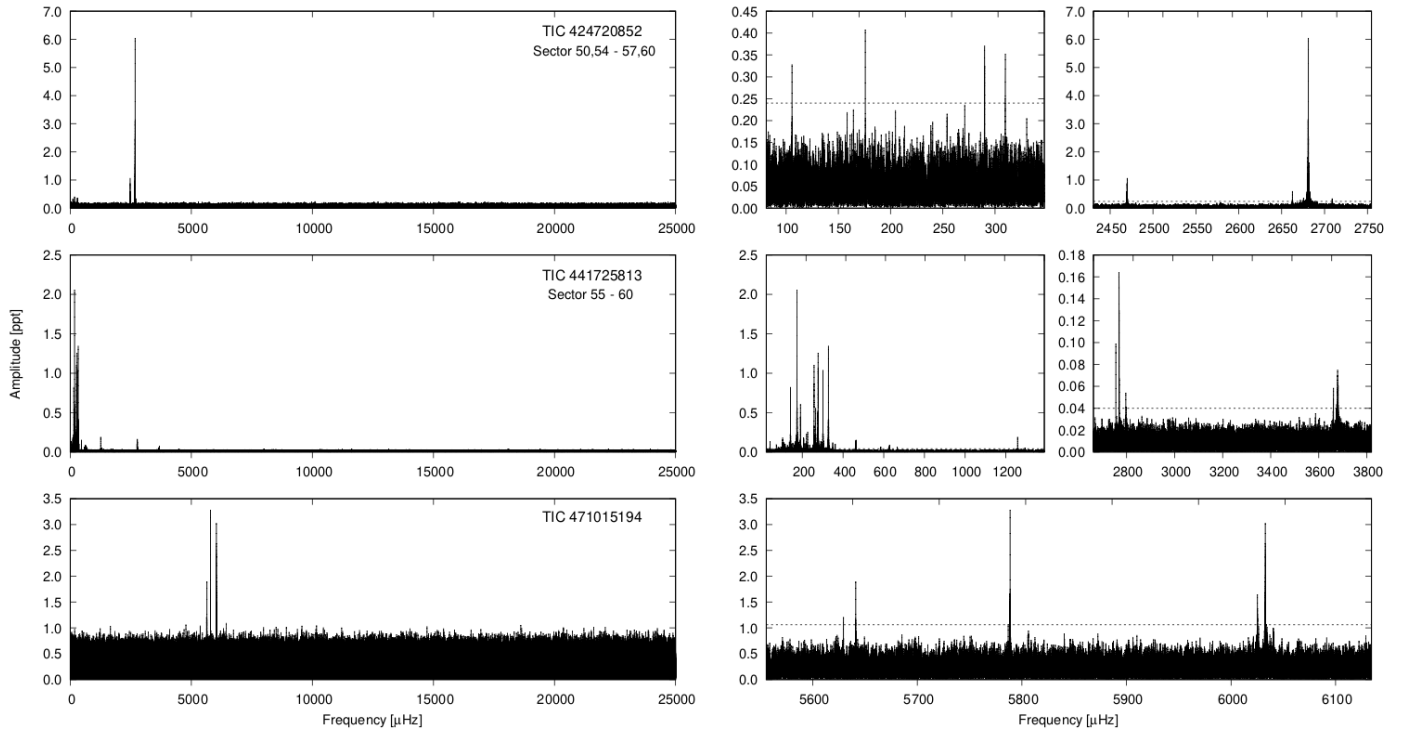


Fig. A.6. Same as in Fig. 2, but for another three targets observed in the USC mode.